Predicting dislocation density in martensite ab-initio

Andric, Predrag; Echeverri Restrepo, S.; Maresca, Francesco

Published in:
Acta Materialia

DOI:
10.1016/j.actamat.2022.118500

Publication date:
2023

Acta Materialia 243 (2023) 118500

Contents lists available at ScienceDirect

Acta Materialia

journal homepage: www.elsevier.com/locate/actamat

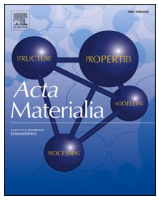

Predicting dislocation density in martensite ab-initio

Predrag Andric [*,a], Sebastián Echeverri Restrepo [a,b], Francesco Maresca [c]

[a] SKF Research & Technology Development (RTD), SKF B.V., Meidoornkade 14, Houten, 3992 AE, the Netherlands
[b] Department of Physics, King's College London, Strand, London WC2R 2LS, United Kingdom
[c] Engineering and Technology Institute (ENTEG), Faculty of Science and Engineering, University of Groningen, Groningen 9747AG, the Netherlands

A B S T R A C T

The high dislocation density (ρ_d) in Fe-C and/or Fe-N martensite is known to be one of the main causes of its overall yield strength. Experiments indicate that the dislocation density and, therefore, the yield strength of martensite in low and medium C steels, follows a well defined behavior with respect to the background concentration of C (c_o). In the present work, we introduce a model based on the finding that the dislocation density after $\gamma \rightarrow \alpha'$ is sufficiently high to accommodate/trap most of the available interstitials (C or N) within Cottrell atmospheres. We show that the number of interstitials trapped in Cottrell atmospheres scales with the interaction energy between the stress field of the dislocations and the C/N misfit tensor. The new model, which contains no free fitting parameters, shows that the dislocation density scales as $\rho_d \sim c_0^{1/4}$, leading to an extremely good match with experiments across a wide range of C and N concentrations. Therefore, this model sheds light on the mechanistic origin of dislocation strengthening in Fe-C and Fe-N martensite.

1. Introduction

Martensitic steels, strengthened by interstitial solutes such as C or N, are usually characterized by a large yield strength which is achieved at limited cost. Therefore, they are irreplaceable structural materials across many industrial applications. The formation of martensite in steels is obtained by the rapid cooling (quenching) from the austenitization temperature to below the so-called "martensite start" temperature, and is characterized by some distinctive features.

First, the transformation process involves nucleation and growth of a bcc/bct phase (α'-Fe) from the high-temperature $\gamma -$ Fe austenite phase (fcc) [1]. In the absence of auto-tempering, the fcc-bcc transformation is diffusionless, thus the interstitials are trapped in solid solution at concentrations much larger than thermodynamic equilibrium in α-Fe [2]. In the solid solution, the interstitial elements occupy the bcc octahedral (OH) sites [3,4].

Second, because of the crystallographic symmetries and large shape deformations that accompanies the phase transformation [2,5], a hierarchical microstructure forms [6] (see Fig. 1a). A prior austenite grain is divided into packets consisting of the plates (laths) that share approximately the same habit plane. Each packet can be further subdivided into three blocks, each one consisting of laths from the same Bain group [6,7]. A block consists of two sub-blocks, each one collecting laths of the same variant. Because of the large shape change that accompanies the $\gamma \rightarrow \alpha'$ transformation, the microstructure of lath martensite is characterized by a large dislocation density, typically in the order of $10^{14} - 10^{15}\mathrm{m}^{-2}$. Such a high dislocation density was found to be dependent on the background concentration of C and N [8–15]. However, while the magnitude of the shape deformation due to the transformation was found to be strongly dependent on the fcc to bcc lattice ratio [2,5], which is a function of the martensite chemical composition, a clear theoretical link between the dislocation density and C/N concentration is missing.

Third, immediately after the $\gamma \rightarrow \alpha'$ transformation and/or during room temperature aging and auto-tempering, interstitials will diffuse towards the dense dislocation network, giving rise to "Cottrell atmospheres" [17]. The migration of interstitials is a thermodynamic process enabled by the generally easy diffusion of C and N in the dislocation-rich martensite [18,19], and driven by the overall reduction in the total energy [20]. In other words, the high energy cost associated with interstitial elements in the solid solution will be minimized by their diffusion towards the attractive sites in the vicinity of dislocations. The formation and existence of Cottrell atmospheres in martensite has, ever since, been experimentally confirmed by several independent groups [21–24]. Using atom-probe tomography (APT) in conjunction with field ion microscopy, Wilde et al. [21] identified C enrichment around dislocations in three different low carbon martensitic steels. They measured the concentration within the atmosphere to be in the order of 8 at% extending to a distance of $\sim 7 \pm 1$nm from the core. Similar results have been found on a different alloy (medium C - Mn steel) [24], whereby

* Corresponding author.
E-mail addresses: predrag.andric@skf.com (P. Andric), f.maresca@rug.nl (F. Maresca).

https://doi.org/10.1016/j.actamat.2022.118500
Received 25 July 2022; Received in revised form 20 October 2022; Accepted 4 November 2022
Available online 13 November 2022

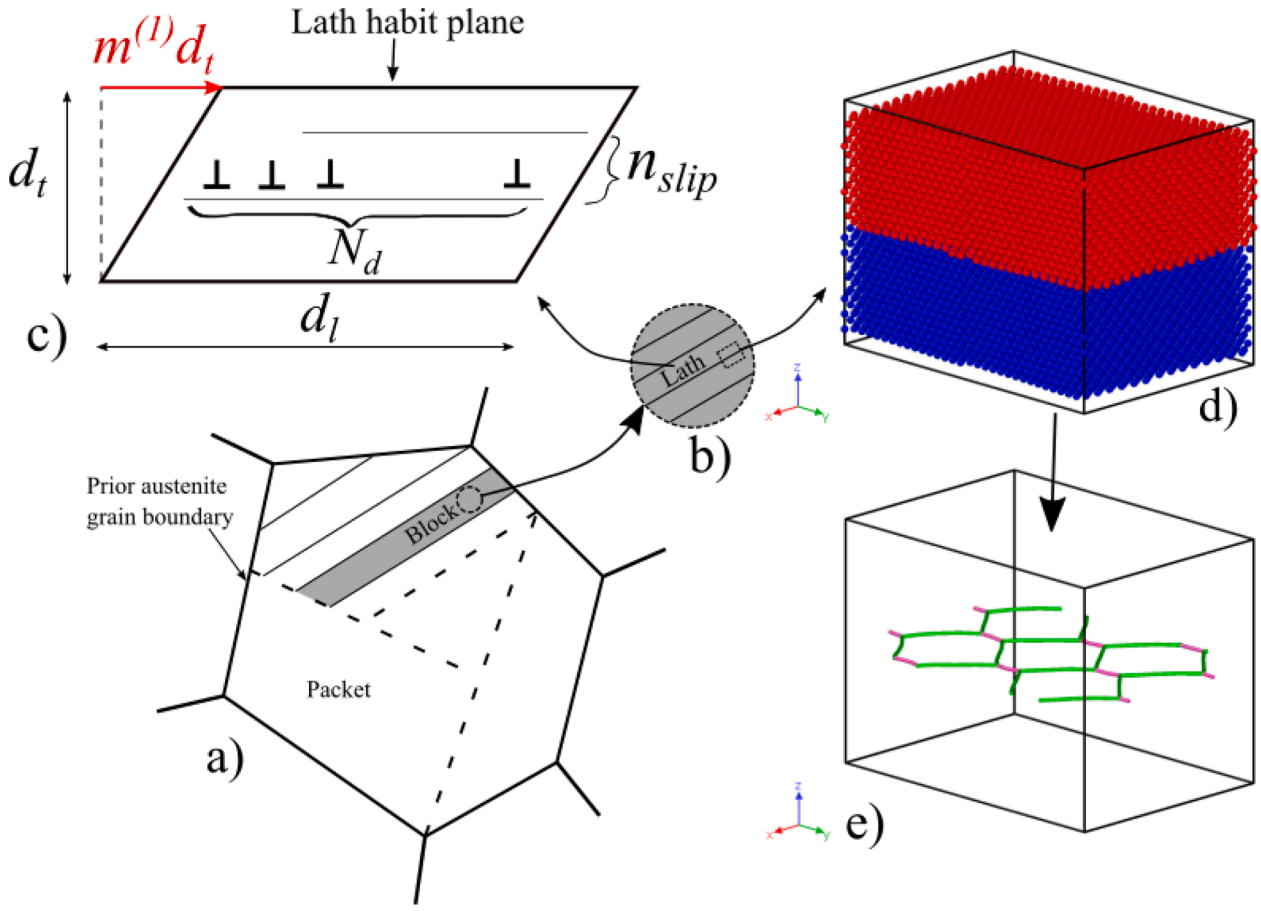

Fig. 1. a) Schematic illustration of the hierarchical microstructure of lath martensite in the Fe-C(N) system. During the austenite to martensite transformation, prior austenite grains are divided into packets (dashed lines), which are further divided into blocks (solid lines within one packet). b) Every block can be divided into laths of the same variant [6]. c) Shape deformation $m^{(1)}$ of a single lath having the length d_l and thickness d_t. According to the martensite transformation theory [2] the shape deformation acts close to to the lath length direction. Number of pile-up dislocations along a single slip plane is indicated by N_d while n_{slip} represents the number of pile-up (slip) planes within a lath area. d) Atomic structure used for simulating a lath boundary. e) Dislocation structure along a low angle twist boundary between two laths. Image adapted from Echeverri Restrepo et al. [16] (Courtesy of Junbiao Lai).

combining ATP with radial integral method 113/1nm C atoms were counted within a 5nm radius region around the dislocation core. Atomistic modeling of Cottrell atmospheres, using a combination of Monte-Carlo and Molecular Statics simulations, have been carried out by Veiga et al. [25]. By using an EAM Fe-C interatomic potential [26], that reproduces reasonably well the DFT symmetric and compact screw dislocation core and Fe-C and C-C interactions, they were capable of modeling the concentration of C around the core with reasonable accuracy compared to the experiments.

Overall, these findings suggest a specific correlation between the C/N concentration and (i) transformation strain magnitude, (ii) the formation of Cottrell atmospheres, (iii) the corresponding dislocation density, and (iv) the martensite microstructure (lath size). However, a fully derived mechanistic theory capable to describe this correlation is still missing. A recent progress, made by Galindo-Nava and co-workers [27], provided a simple model for estimating the dislocation density and lath size as a function of C concentration. However, the quantitative accuracy of the model is limited (see Section7 for more details) even though their predictions do follow general experimental trends.

The reminder of the paper is organized as follows. Analytical methods and general thought process used in the manuscript are described in Section 2. In Section 3 we find the correlation between C concentration and transformation strain magnitude, and initial dislocation density. Atomistic validation of the screw dislocation annihilation immediately after $\gamma \rightarrow \alpha'$ transformation is presented in Section 4. In Section 5 we derive a closed form solution for calculating the final dislocation density as a function of the interstitials concentration and temperature. In Section 6 we compare the predicted size of the Cottrell atmosphere and the new model for dislocation density with the available experimental results. Implications of the new model are discussed in Section 7. Finally, our main results are reiterated in Section 8. Throughout the article, we use Cartesian coordinates with the axes labeled as x_i $(i = 1,2,$ or $3)$. The Einstein's summation convention over repeated indices is used.

2. Analytical methods

Here, we deal with the problem of estimating dislocation density ρ_d versus C/N concentration by modeling the martensitic transformation through several distinctive steps:

(i) We predict the magnitude of the $\gamma \rightarrow \alpha'$ *in-situ* transformation strain (i.e. shape deformation) as a function of the lattice parameter ratio $r = a_{fcc}/a_{bcc}$ between fcc and bcc, which itself is a function of C/N concentration, by using the parameter-free crystallographic theory of martensite [2]. The calculated transformation strain was shown to be approximately 60% for a wide range of C concentrations ($0.01 < c_0 < 0.6$) wt% within the prior austenite. In other words, the magnitude of $\gamma \rightarrow \alpha'$ transformation strain is shown to be large (as expected) but weakly dependent on the C concentration within this range of compositions.

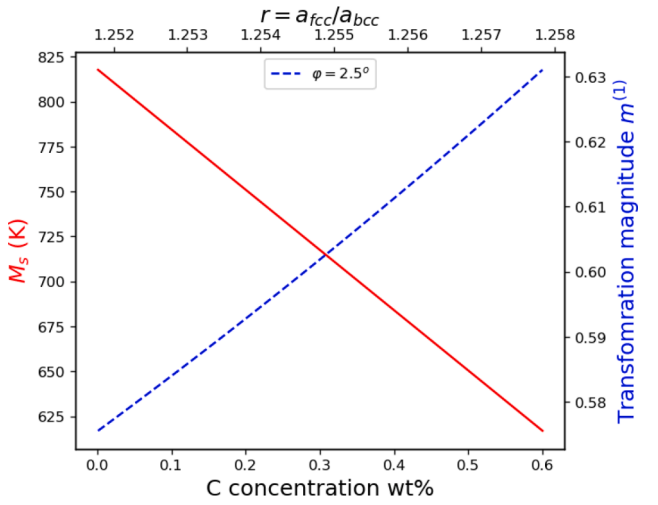

Fig. 2. Martensite start temperature (M_s) (solid red line) and magnitude of the transformation strain $m^{(1}$ (dashed blues line) as a function of the C concentration in wt % or fcc to bcc lattice parameter ratio $r = a_{fcc}/a_{bcc} = f(c_0, M_s)$. (For interpretation of the references to colour in this figure legend, the reader is referred to the web version of this article.)

(ii) The initial dislocation density ρ_d^{ini} *immediately after* the $\gamma \rightarrow \alpha'$ transformation is then calculated assuming a linear distribution of dislocations on a slip plane [28–31]. The calculated ρ_d^{ini} immediately after transformation is shown to be directly proportional to the magnitude of the transformation strain, and therefore weakly dependent on the C concentration as well. More importantly, the calculated ρ_d^{ini} is shown to be compatible with the dislocation density measured in medium and high C steels ($c_0 \gtrsim 0.3$wt%), and generally larger than the dislocation density measured in low C steels ($c_0 \lesssim 0.3$wt%).

(iii) Finally, starting from the initial dislocation density ρ_d^{ini}, we show that the final dislocation density ρ_d will reduce to a value sufficiently large such that most interstitial atoms are trapped by the Cottrell atmosphere while all the excess dislocations, formed upon transformation, are annihilated ($\rho_d \leq \rho_d^{ini}$). The annihilation of excess dislocations immediately after $\gamma \rightarrow \alpha'$ transformation is more pronounced in low C steels due to weaker dislocation strengthening by C in solid solution. We tackle pinning of dislocations by formation of Cottrell atmosphere by considering the interaction energy between the dislocation and the C/N misfit. The misfit tensor represents a volume and shape change of the host lattice (bcc lattice) when a single interstitial element is introduced, and the lattice is allowed to fully relax. The same concept has been successfully applied in various problems such as solute strengthening in fcc [32,33] and bcc metals [34], hydrogen embrittlement [35,36], and stress driven diffusion [37,38]. We then show that the number of C/N atoms trapped in Cottrell atmospheres N_C scales with the interaction energy between a dislocation and the C/N misfit tensor, leading to a well-defined relationship between N_C and the background concentration c_0. The dislocation density ρ_d is then shown to be directly proportional to C/N concentration and inversely proportional to N_C.

The closed-form solution for ρ_d is derived and the model is validated against experiments, obtaining an excellent agreement. The new model captures the scaling of the dislocation density with the C/N concentration. Finally, the model is used to clarify the experimental correlation between the C concentration and martensite lath size and strength. This problem is addressed by using a bottom-up approach, where the macroscopic properties of martensite are derived by working out the interaction of dislocations with surrounding point defects/solutes.

3. The role of the transformation strain on the initial, metastable dislocation density of martensite

The parameter-free theory of martensite crystallography [2] enables to predict the full shape deformation tensor $\mathbf{P}^{(1)}$ of lath martensite as a function of the fcc/bcc lattice parameter ratio $r = a_{\text{fcc}}/a_{\text{bcc}}$ and the fcc/bcc orientation relationship. The shape deformation is an invariant-plane strain which can be written in the form

$$\mathbf{P}^{(1)} = \mathbf{I} + m^{(1)}\mathbf{s}^{(1)} \otimes \mathbf{n}^{(1)} \tag{1}$$

where $\mathbf{I}$ is the second order identity tensor, $m^{(1)}$ is the shape deformation magnitude, $\mathbf{s}^{(1)}$ the transformation direction and $\mathbf{n}^{(1)}$ the habit plane normal. The shape deformation magnitude $m^{(1)}$ in Eq. (1) is

$$m^{(1)} = \lambda_{\max} - \lambda_{\min} \tag{2}$$

where $\lambda_{\max}$ and $\lambda_{\min}$ are, respectively, the largest and the smallest eigenvalues (principal stretches) of $\mathbf{U} = \sqrt{[\mathbf{P}^{(1)}]^T \cdot \mathbf{P}^{(1)}}$. The intermediate eigenvalue of $\mathbf{U}$ equals 1 because $\mathbf{P}^{(1)}$ is an invariant-plane strain. Operationally, $\mathbf{U}$ is computed by using the decomposition

$$\mathbf{P}^{(1)} = \mathbf{R}_\Delta \cdot \mathbf{R} \cdot \mathbf{B} \cdot \mathbf{P}^{(3)} \cdot \mathbf{P}^{(2)} \tag{3}$$

where $\mathbf{R}_\Delta$ (far-field micro-rotation) and $\mathbf{R}$ (rotation associated with the orientation relationship at the interface) do not affect $\mathbf{U}$ and hence $m^{(1)}$, as it can be verified easily by substitution of Eq. (3) in the expression of $\mathbf{U}$. $\mathbf{P}^{(3)}$ is a lattice-invariant shear deformation that is carried by an array of interface screw dislocations, and its magnitude is such that the intermediate eigenvalue of $\mathbf{U}$ is unity. $\mathbf{B}$ is the "Bain strain" deformation tensor, which can be expressed in matrix form as

$$[\mathbf{B}] = \begin{bmatrix} \frac{\sqrt{2}}{r} & 0 & 0 \\ 0 & \frac{\sqrt{2}}{r} & 0 \\ 0 & 0 & \frac{1}{r} \end{bmatrix} \tag{4}$$

and hence depends solely on the lattice parameter ratio r. Finally, $\mathbf{P}^{(2)}$ is a second set of lattice-invariant shears, the magnitude of which depends explicitly on the orientation relationship at the interface, which is indicated by a misorientation angle φ between Kurdjumov-Sachs and Nishiyama-Wassermann. Therefore, the shape deformation magnitude depends solely on φ and r. It has been shown that, in low-C steels, $\varphi \simeq 2.5^\circ$ [39]. We can therefore predict $m^{(1)}$ as a function of r only.

In low-C steels, $r = a_{fcc}/a_{bcc}$ is calculated using the experimentally measured lattice parameters of $\alpha - \text{Fe}$ and $\gamma - \text{Fe}$ versus C concentration and temperature [40] expressed in the empirical form as

$$a_{fcc}(T, c_0^{wp}) = (0.36306nm + 0.00078nm \cdot c_0^{wp}) \times \left[1 + (24.9 - 0.5 \cdot c_0^{wp}) \cdot 10^{-6} \cdot (T - 1000K)/1K\right] \tag{5a}$$

$$a_{bcc}(T) = 0.28863nm \cdot \left[1 + 17.5 \cdot 10^{-6} \cdot (T - 800K)/1K\right] \tag{5b}$$

where c_0^{wp} is the C concentration expressed in the weight percent, and T is the temperature in K. We focus on C since there are more available data, yet the analysis is general and applies to N as well. As for the temperature effect on r, we use the martensite start temperature (M_s) which is also a function of the C concentration. Fig. 2 shows M_s as a function of the C concentration calculated using the commercial software Thermo-Calc [41]; the well-known linear reduction of M_s with increasing C is obtained. We now calculate the magnitude of $\gamma \rightarrow \alpha'$ transformation strain $m^{(1)}$ as a function of r and C concentration

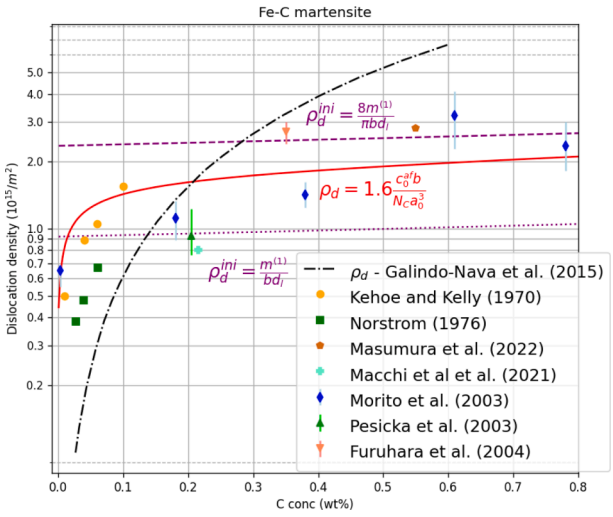

Fig. 3. Dislocation density immediately after $\gamma \rightarrow \alpha'$ transformation ρ_d^{ini} calculated using $d_l = 10 \times 0.25\mu m = 2.5\mu m$ with Eqs. (12) and 13 (purple dashed and dotted lines, respectively). The final dislocation density calculated using Eq. (19) (red solid line) at $T = 300$K as a function of the C concentration in Fe-C martensite. Results are compared against the available TEM based measurements of dislocation density [8–14] and with the recent model of Galindo-Nava et al. [27] (black dashed-dotted line). (For interpretation of the references to colour in this figure legend, the reader is referred to the web version of this article.)

$0.001 < c_0 < 0.6$wt% (see Fig. 2), and reveal a couple of interesting features.

First, Fig. 2 shows a very large magnitude of the transformation strain ($m^{(1)} \approx 60\%$). Second, although $m^{(1)}$ is large as anticipated, it is weakly dependent on the C concentration within contents relevant to lath martensite. The transformation strain $m^{(1)}$ is accommodated by the initial dislocation network, the density of dislocations which is indicated as ρ_d^{ini}. To connect C concentration and dislocation density due to the $\gamma \rightarrow \alpha'$ transformation, we compute ρ_d^{ini} due to $m^{(1)}$ by using the method of linear distribution of dislocations [28–31]. Thus, we consider a slip plane embedded within an isotropic single crystal (the martensite) of size d and parallel to the $x_1 - x_3$ plane such that the slip plane normal points into the x_2 direction and the dislocation line is aligned with the x_3 direction. The $\gamma \rightarrow \alpha'$ transformation generates a distribution of dislocations on the slip plane (see Fig. 1c)) having *line density* $D(x_1)$ (number of dislocations per unit line). The dislocation array is in equilibrium when

$$\tau_d + \Delta\tau = 0 \tag{6}$$

where τ_d is the dislocation back-stress, while $\Delta\tau = \tau_{ext} - \tau_f$ $(\tau_{ext} > \tau_f)$ is the difference between an external shear stress τ_{ext}, and the stress τ_f arising from the dislocation strengthening by C/N in either solid solution or in Cottrell atmosphere. Note that τ_f is not limited to interstitial elements and can also include the effects of substitutional solutes like e.g. Si, Mn, Ni. The origin of τ_{ext} can be related to either the thermodynamic driving force for $\gamma \rightarrow \alpha'$ transformation, and/or residual stress in the newly formed martensite. Here, we consider $\Delta\tau$ constant and show that the resulting dislocation density is independent of it if $m^{(1)}$ is known; therefore, we do not discuss further its detailed description. The dislocation back-stress due to $D(x_1)$ is then [31]

$$\tau_d = M \int_{-d/2}^{d/2} \frac{D(\eta)}{x_1 - \eta} d\eta \tag{7}$$

where $M = \mu b/2\pi$ for screw dislocations, $M = \mu b/2\pi(1-\nu)$ for edge dislocations, and d is the length of the dislocation pile-up, which is commonly associated with the material grain size. For the problem considered here, d can be envisioned as the lath length $(d = d_l)$, since according to the theory of martensite transformation $m^{(1)}$ is predominantly a shear acting along the lath habit plane close to the lath length direction (see Fig. 1c). Furthermore, b, μ and ν are Burgers vector, shear modulus and Poisson's ratio, respectively. Solving the integral Eq. (7) for $D(x_1)$ yields [29]

$$D(x_1) = \frac{\Delta\tau}{\pi M \sqrt{\left(\frac{d_l}{2x_1}\right)^2 - 1}} \tag{8}$$

when $D(x_1)$ is unbounded at $x_1 = -d_l/2$ and $x_1 = d_l/2$. Thus, integrating the line density (Eq. (8)) between $-d_l/2 < x_1 < d_l/2$ [29,31] yields the total number of dislocations (see Fig. 1 c))

$$N_d = 2\int_0^{d_l/2} D(x_1)dx_1 = \frac{\Delta\tau d_l}{\pi M} \tag{9}$$

which leads to [31]

$$\gamma_{slip} = b\int_{-d_l/2}^{d_l/2} x_1 D(x_1)dx_1 = \frac{\Delta\tau b d_l^2}{8M} = \frac{\pi}{8} N_d b d_l. \tag{10}$$

Multiplying γ_{slip} by the number of pile-up layers n_{slip} in a lath area $S = d_l d_t$, d_t is lath thickness (see Fig. 1 c)), leads to the following connection between transformation strain, total slip and dislocation density:

$$m^{(1)} = \frac{n_{slip}}{S}\gamma_{slip} = \frac{\pi}{8}\rho_d^{ini} b d_l, \tag{11}$$

which yields the dislocation density as

$$\rho_d^{ini} = \frac{n_{slip}}{S} N_d = \frac{8}{\pi}\frac{m^{(1)}}{b d_l} \tag{12}$$

With no free fitting parameters, Eq. (12) provides the correlation between the transformation strain magnitude, lath length and dislocation density, and it is the first main result of this paper.

A similar result can be derived using a simple geometrical estimate (see Fig. 1c)) which shows that for a single, unconstrained crystal that is free to deform, $m^{(1)} = \frac{Nb}{d_t}$ where $N = N_d n_{slip}$ is the total number of dislocations. Since $\rho_d^{ini} = \frac{N}{S}$ and $S = d_t d_l$, then

$$\rho_d^{ini} = \frac{m^{(1)}}{b d_l} \tag{13}$$

which differs from Eq. (12) by a factor of $8/\pi$. This means that, in order to accommodate the same plastic deformation due to a (shear) transformation strain $m^{(1)}$, the dislocation density in a constrained crystal (with rigid grain boundaries) is larger than the dislocation density in a crystal that could freely deform (the dislocations can freely glide through the grain boundaries). We therefore conclude that the actual initial dislocation density is between the free deforming crystal and the crystal with rigid boundaries, hence $\frac{m^{(1)}}{d_l b} \leq \rho_d^{ini} \leq \frac{8}{\pi}\frac{m^{(1)}}{d_l b}$. Thus, the free deformation and rigid grain boundaries set the two bounds for the initial dislocation density. We envision that the rigid boundary limit might be closer to reality, since lath boundaries are characterized by a dense network of misfit dislocations, and possibly secondary retained phases (austenite, or carbides) that might hinder slip transfer.

Interestingly, we notice the similarity of Eqs. (11) and (13) with the Orowan equation $\dot{\gamma} = \rho_d b v$, where $\dot{\gamma}$ is the strain rate and v is the dislocation speed. It is easy to see that time differentiation of Eq. (11) leads to the Orowan equation where $v = const$ can be envisioned as the time needed for a single dislocation to travel the mean slip length equal to either $\pi d_l/8$ or d_l (constrained vs free crystal, respectively).

The dashed and dotted purple lines in Fig. 3 show ρ_d^{ini} calculated as a function of the $m^{(1)}$ (or C content) and using Eqs. (12) and 13, respectively. Since the lath length is usually not reported in the literature, we

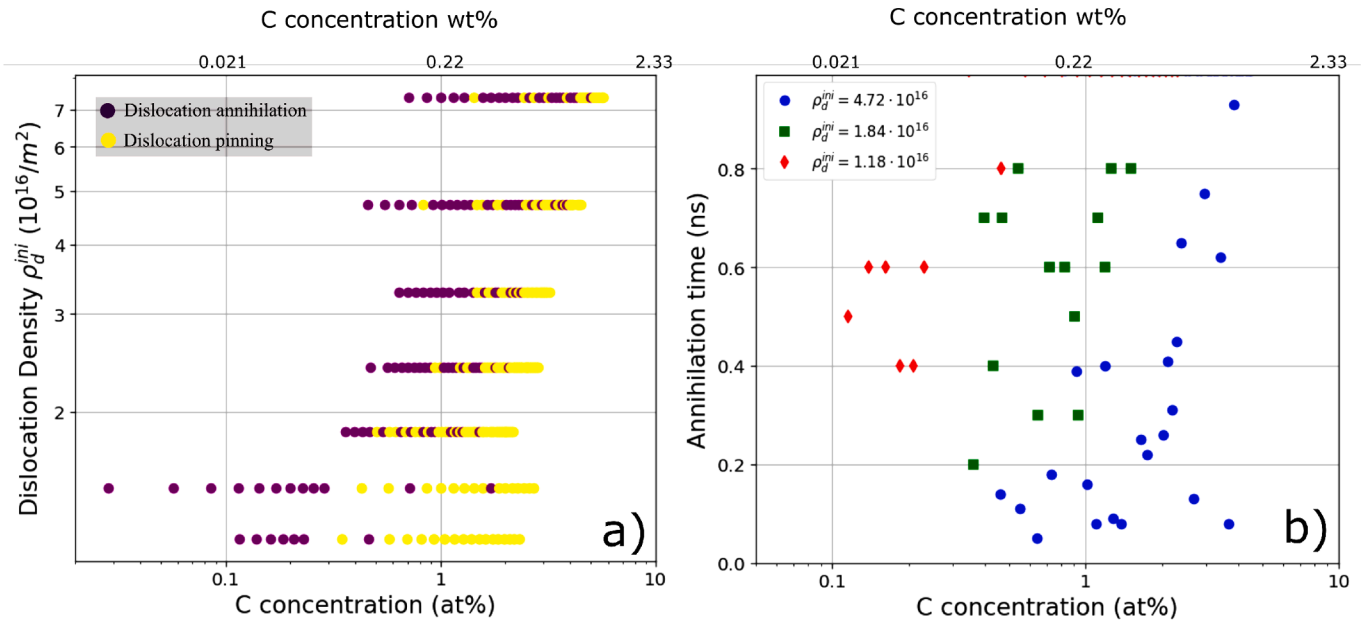

Fig. 4. a) Competition between screw dislocation annihilation (purple circles) and dislocation pinning (yellow circles) as a function of C concentration in solid solution and initial dislocation density. b) Annihilation time as a function of the C concentration for three different levels if the initial dislocation density. The results are obtained using Molecular dynamics simulations with Fe-C EAM interatomic potential [26]. (For interpretation of the references to colour in this figure legend, the reader is referred to the web version of this article.)

estimate it using the typical lath thickness across the range of C concentrations ($d_t \approx 0.25\mu$m, see Fig. 11) and we multiply it by a factor of 10 leading to $d_l \approx 10d_t \approx 2.5\mu$m, which is consistent with transmission electron microscopy (TEM) micrographs [42]. The estimated ρ_d^{ini} (see Fig. 3) points to several interesting observations. First, the shape change due to martensite formation leads to a large dislocation density, as expected; $\rho_d^{ini} \sim 2.54{\cdot}10^{15}\ 1/m^2$ when calculated using Eq. (12), and $\rho_d^{ini} \sim 0.99{\cdot}10^{15}\ 1/m^2$ when calculated using Eq. (13). Essentially, the two calculated values for ρ_d^{ini} are an upper and lower bound, as already indicated above. Second, ρ_d^{ini} increases with increasing C content, which is a direct consequence of $m^{(1)}$. Third, while ρ_d^{ini} increases with C content, its change is rather weak because $m^{(1)}$ is weakly dependent on C. Fourth, using Eq. (12) for calculating ρ_d^{ini} leads to a generally better prediction compared to the experiments in lath martensite, especially for $c > 0.1$wt % of C (see Fig. 3); therefore, the experimental measurements tend to be closer to the upper bound on ρ_d^{ini} suggesting that the assumption of rigid grain boundaries is closer to the real conditions. This conclusion is physically sound because, unlike the free deforming crystal, the rigid grain boundary approximation can be envisioned as a grain constrained by a surrounding material. Finally, the calculated ρ_d^{ini} (Eq. (12)) is generally bigger than the measured one, and most importantly, its dependence on C content does not follow the experimental trend in low C martensite (see Fig. 3). At first, this result appears to be significantly off even though Eq. (12) is robust and depends solely on basic material properties. We therefore argue that dislocations created after the $\gamma{\rightarrow}\alpha'$ undergo (i) dislocation annihilation and (ii) dislocation pinning by formation of Cottrell atmospheres. Dislocation annihilation is expected to occur since a large fraction of dislocations are of screw character [43]. Furthermore, this process is expected to be more pronounced in low-C martensite due to weak strengthening by C in solid solution. The dislocation pinning by Cottrell atmospheres is enabled by a very fast diffusion of C and/or N towards dislocations in dislocation-rich martensite [19]. Both processes are driven by the reduction of the total energy and can occur at finite temperatures (i.e. room temperature annealing). We discuss the implication of dislocation annihilation due to annealing on the dislocation density in the next Section.

4. Atomistic modeling of screw dislocation annihilation in α – iron

A tendency for thermally activated dislocation annihilation during tempering [14,44], plastic deformation [45–47] and creep [12,48] has been observed experimentally by several independent groups. However, the experimental basis for dislocation annihilation immediately after $\gamma{\rightarrow}\alpha'$ transformation is not available. To provide validation to our assumption on annihilation of screw dislocations, we employ classical molecular dynamics (MD) simulations. More specifically, we model the effect of initial dislocation density and C concentration on screw dislocation annihilation at finite temperatures. Fe-C interactions are described by using the EAM potential developed by Becquart et al. [26]. A single bcc-Fe crystal is generated and oriented with $x_1 = [1\ 2\ \bar{1}]$, $x_2 = [1\ 0\ 1]$ and $x_3 = [1\ \bar{1}\ \bar{1}]$. Then, a quadrupole of screw dislocations, having the dislocation line $\boldsymbol{\xi}$ along x_3 and Burgers vector $\boldsymbol{b} = [0,\ 0,\ b]^T$ or $\boldsymbol{b} = [0,\ 0,\ -b]^T$, is inserted in the simulation box by imposing the anisotropic displacement field for each dislocation separately (see Eq. (A.2)). The system is relaxed to recover lattice periodicity in all three directions. Since the dislocation density can be related to average dislocation spacing via $\rho_d^{ini} = 1/l^2$, we model ρ_d^{ini} by keeping the fixed number of dislocations (four) and by changing both the simulation box size in x_1 and x_2 directions and hence the spacing between the dislocations. The size of the simulation box along x_3 direction is kept constant and equal to 6 Burgers vectors. Finally, to simulate the effect of C concentration on dislocation annihilation, we insert a different number of C atoms into the simulation box leading to concentrations within the range $c_0^{ac} = 0.2 - 6$ at.%. Classical MD simulations are run for 1ns with a Langevin thermostat [49,50] (damping factor of 0.1ps) in a NVE ensemble at 725K. The simulated temperature corresponds to the M_s temperature in medium C steels (see Fig. 2). At a given dislocation density, we perform between 25 and 50 simulations at different C concentrations, leading to a total of 280 MD simulations.

The results presented in Fig. 4 confirm our main assumption, that dislocations can easily annihilate at low C contents. Figure 4a) shows the competition between the dislocation annihilation (purple circles) and dislocation pinning (yellow circles) as a function of the C concentration,

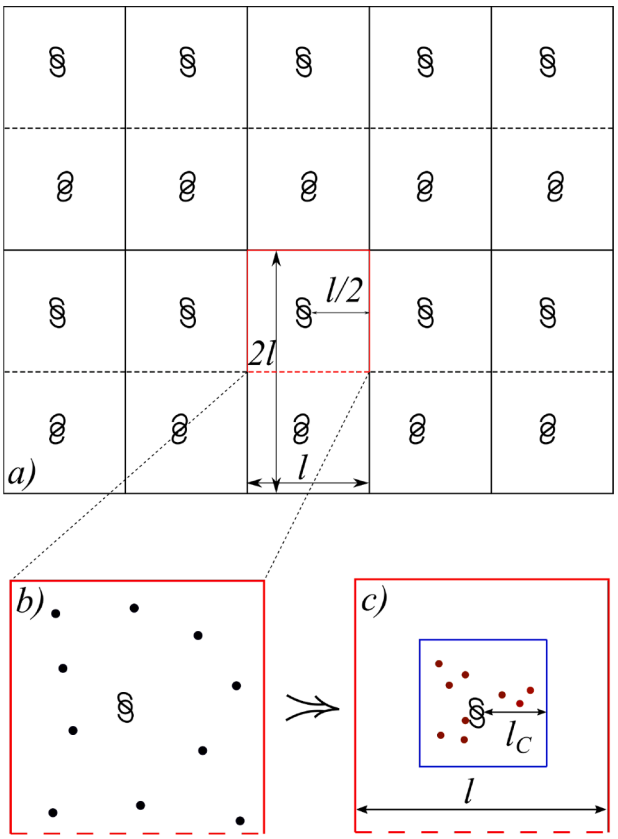

Fig. 5. a) Periodic dislocation structure with average spacing between the dislocations l, and the corresponding dislocation density $\rho_d = 1/l^2$. b) Sub-unit cell of size $l \times l$ immediately after austenite to martensite transformation. Interstitial atoms are randomly distributed in solid solution and the probability of finding one of them is equal to the background concentration. c) Distribution of interstitials within a Cottrell atmosphere of size l_C after diffusion of interstitials towards dislocation takes place.

and the initial dislocation density after ($t = 1ns$). First, with reduction of the C concentration, and with increase of the initial dislocation density, the dislocation annihilation is more likely to occur. The phenomenon of dislocation annihilation is driven by the easy cross-slip of screw dislocations, which dominate low-alloyed bcc metals such as martensite in steel [43]; in other words, the quadrupole screw dislocation structure is unstable, and it can change towards a lower-energy structure at finite temperature. Second, at a given initial dislocation density and simulation time of $1ns$, there is a transition concentration at which dislocation annihilation is less likely to occur (see Fig. 4 and change from purple to yellow color); the transition concentration reduces with the reduction of the initial dislocation density, as expected. However, at longer time scales, that match more closely with the experimental martensite formation, it is reasonable to expect that the transition zone is shifted towards the higher C concentrations. Third, using the Fe-C EAM potential [26] we find that the annihilation of excess dislocations is an extremely fast process ($t < 1ns$) and it is therefore very difficult to observe experimentally. To gain more insight into the dislocation annihilation rate, we examine the annihilation times for three different levels of the initial dislocation density ρ_d^{ini} (see Fig. 4b). At a fixed C concentration, the annihilation of dislocations occurs at a much faster rate as ρ_d^{ini} is high, and vice-versa, as expected. A similar trend can be also associated with the reduction of the C concentration which generally leads to a shorter annihilation times. However, we do observe a more significant data scattering which is a direct consequence of the randomness of the initial dislocation-C structure. Finally, for the simulation time used here, we do not observe the formation of Cottrell atmosphere suggesting that this process takes longer time compared to the annihilation of dislocations. However, as the annihilating rate slows down with the reduction of the dislocation density, the formation of Cottrell atmospheres takes place in the later stage of the process.

Despite the lack of experimental observations, the MD results presented here clearly suggest that annihilation of the initially high dislocation density is very likely to occur. As already pointed out above, the process of dislocation annihilation is more likely to occur at lower C concentrations and high dislocation densities. Therefore, we conclude that the deviation between Eq. (12) and the experiments for low C steels is a consequence of the dislocation annihilation. In the next Section, we show that the final dislocation density in lath martensite is primarily controlled by the number of interstitial atoms (C or N) trapped by dislocations (Cottrell atmospheres). Therefore, the problem is controlled by the (long-range) interaction of individual dislocations with interstitial solutes.

5. Model for dislocation density in martensite

5.1. Connection between C content and dislocation density

Consider a representative unit cell of a material with volume $V = l \times 2l \times L$, where l and $2l$ represent dimensions in the $x_1 - x_2$ plane, while L is the thickness along the x_3 axis, aligned with the dislocation lines. Since we focus on individual dislocations, the boundary conditions are chosen to be periodic along all three directions. We then assume that the representative volume V has undergone an instantaneous phase transformation from austenite to martensite ($\gamma \rightarrow \alpha'$). Immediately after the transformation, the interstitial solutes are randomly distributed in the matrix since the $\gamma \rightarrow \alpha'$ transformation is diffusionless [2,51]; in other words, the probability of finding an interstitial in an OH site *immediately* after the $\gamma \rightarrow \alpha'$ transformation is equal to the average C concentration c_0 (see Fig. 5b). The above assumption is reasonable since the dislocation density in the parent austenite can be neglected due to the high austenitization temperatures. The number of interstitial atoms in the representative volume V is

$$N_i = 6c_0\frac{V}{a_0^3} = 6c_0\frac{2l^2L}{a_0^3} \tag{14}$$

where 6 is the number of OH sites in a unit cell (bcc) and, $c_0 \ll 1$ is the background atomic fractional occupancy of an interstitial site and it is related to the background atomic concentration c_0^{af} via $c_0 = c_0^{af}/3$ ("af" stands for atomic fraction). Furthermore, the $\gamma \rightarrow \alpha'$ transformation leads to the formation of an initial dislocation structure with density ρ_d^{ini} (see Section 3 and dashed purple line in Fig. 3). For the sake of simplicity, we assume that the initial distribution of dislocations can be modeled as a periodic lattice of dislocation dipoles with dislocation lines ξ lying along x_3. We used the similar structure in Section 4 since it enables energy reduction through the cross slip annihilation mechanism. Note that one dislocation array of the same sign corresponds to the structure studied in Section 3; those dislocations can be envisioned to belong to one slip plane. Figure 5a shows a schematic representation of the domain in which every unit cell contains a dislocation dipole. Within the adopted dislocation structure, every unit cell can be divided into two sub-unit cells ($l \times l \times L$) containing a single dislocation, leading to the corresponding initial dislocation density $\rho_d^{ini} = 1/l_{ini}^2$ for the initial dislocation separation $l = l_{ini}$. The total energy of the volume V is:

$$E_1 = E_d(l_{ini}) + E_{\text{img}}(l_{ini}) + \sum_{i=1}^{Ni} E_i \tag{15}$$

where E_d is the elastic energy due to the dislocation dipole in the unit cell, E_{img} is the interaction energy between the dipole and all the periodic images, and $\sum_{i=1}^{Ni} E_i$ is the sum of the excess energy due to the lattice

Table 1
Calculated misfit tensors of C and N in $\alpha-$ Fe. The computational details are given in Appendix Appendix C. The units of the misfit tensors are expressed in Å^3.

	Ω_{11}	Ω_{22}	Ω_{33}	$\Delta\Omega$
C	-0.55	-0.55	11.45	10.34
N	-0.13	-0.13	11.07	10.81

distortions caused by the interstitial solutes. The periodic image interaction between the point defects can be safely neglected (i) because $c_0 \ll 1$ and (ii) due to the short range nature of the point defect stress field ($\sim 1/x^3$) (x distance from the point defect). In addition, the interaction energy between a dislocation and the interstitials equals zero due to the random distribution of solutes and the symmetry of the stress field: thus, the mean interaction energy is zero [32,52].

At this point, there is a high energy cost associated with E_1 due to (i) the very high initial dislocation density ρ_d^{ini} (formed upon $\gamma \rightarrow \alpha'$ transformation), and (ii) the big lattice distortions caused by the interstitial elements (C or N, see Table 1), which are in solid solution at concentrations well above the saturation value for α-Fe. The high total energy E_1 is then minimized in low-C steels by the two distinctive phenomena: (i) annihilation of dislocations by cross-slip, followed by (ii) diffusion of interstitials towards the attractive OH sites around the dislocation, leading to the formation of Cottrell atmospheres. The first phenomenon is driven by the easy cross-slip of screw dislocations as suggested by MD simulations in Section 4. The second process is enabled by the reduced annihilation rate at lower ρ_d^{ini} (see Fig. 4b)) and it is driven by the long-range interactions between the dislocations and interstitials. The annihilation process is then completely stopped due to dislocation pinning by the newly formed Cottrell atmospheres. Therefore, the final total energy reaches *local equilibrium* (see Fig. 5c)

$$E_2 = E_d(l) + E_{\text{img}}(l) + \sum_{i=1}^{Ni} E_i - 2\sum_{j,\ k} E_b\left(x_1^j,\ x_2^k\right) \tag{16}$$

where E_b is the contribution of the dislocation-solute interaction energy, where the factor 2 is due to the dislocation dipole. The interaction energy between the dislocation and a solute positioned at $(x_1,\ x_2)$ with respect to the dislocation line is calculated as

$$E_b(x_1,\ x_2) = -\sigma_{ij}^d \Omega_{ij} \tag{17}$$

where σ_{ij}^d is the dislocation stress tensor at $(x_1,\ x_2)$ (see Appendix A) while Ω_{ij} is the solute misfit tensor. Note that both the stress and the misfit tensor need to be expressed with respect to the same coordinate system when E_b is evaluated. From a thermodynamic point of view, for a solute atom sitting at a position (x_1, x_2) with respect to the dislocation core, a positive interaction energy indicates a reduction in the total energy compared to the system in which the solute is far from the dislocation. A detailed derivation of Eq. (17) is given in Appendix A.

After relaxation, the interaction term is nonzero because the interstitial atoms are biased towards the positive (attractive) OH sites. The term "equilibrium" used above does not correspond to the thermodynamic equilibrium of $\alpha-$ Fe, but rather to a local energy minimum achieved by the formation of Cottrell atmospheres.

The diffusion of the interstitials towards the dislocation occurs immediately upon quenching (auto-tempering) and/or during room-temperature (low-temperature) aging, as confirmed experimentally [21]. As a result, the final energy state corresponds to the dislocation density $\rho_d \leq \rho_d^{ini}$ that is sufficiently large to capture most of the excess interstitial elements in solid solution to the Cottrell atmospheres of size l_C (see Fig. 5c). In other words, due to dislocation annihilation, the energy E_1 is minimized with respect to $l,\ l > l_{ini}$ until all the interstitials are trapped within l_C. By taking $L = \zeta = b$ and using mass conservation, the above minimization yields

$$N_C = \frac{6 f c_0 l^2 b}{a_0^3} \tag{18}$$

where N_C is the number of interstitial atoms captured by the Cottrell atmosphere, and f is an experimental correction coefficient for the fraction of interstitials that stays in the solid solution. A reasonable estimate is $f = 0.8$, based on the experimental finding that approximately 20% of the interstitials do not to diffuse towards the dislocations [21]. Using $l^2 = 1/\rho_d$, and $c_0 = c_0^{\text{af}}/3$,

$$\rho_d = 1.6 \frac{c_0^{\text{af}} b}{N_C a_0^3} \tag{19}$$

which is the relation that enables calculating the dislocation density in interstitially strengthened martensite. This is the second main result of this article. Additional minimization of the total energy due to cross-slip annihilation, and therefore reduction in the dislocation density, might be possible either because of reduced diffusivity of interstitials (slower formation of Cottrell atmospheres), by precipitation of cementite or by C enrichment of retained austenite [53], which are not considered here. Therefore, Eq. (19) is an upper bound for the dislocation density, since it is based on the assumption that all remaining dislocations in the laths are fully saturated with interstitials.

Finally, a significant fraction of interstitials also diffuses towards the lath boundaries in lath-martensite. However, the above simple dislocation structure remains valid, since the low-angle lath boundaries are usually of the twist character [54] and, therefore, the lattice mismatch between them is most likely accommodated by screw dislocations, as confirmed by detailed atomistic simulations [2]. In other words, the model presented here applies to both cases, since it does not differentiate between the dislocations along the lath boundaries and the dislocations within the laths. To validate this assumption we have performed molecular statics simulations of low angle twist boundary between neighboring laths.

To show that even in absence of retained austenite the lath boundary structure reflects that of a screw dislocation network, we employ molecular statics simulations following Refs. [55,56]. Computational details are provided in Appendix B. Figure 1e demonstrates that the lath boundaries are indeed composed of the dislocation network and as such they play a role in the total dislocation density and diffusion of interstitials towards them. This is consistent with TEM analysis by Sandvik and Wayman [43], who image screw dislocations network which could be either within the laths or at lath boundaries.

The above analysis showed that N_C and ρ_d are intimately coupled through the background concentration of interstitials. In the following section we model the temperature-dependent interstitials concentration around dislocations, which is a crucial step to derive the expression for N_C as a function of the interaction energy between dislocations and the interstitials.

5.2. Modeling Cottrell atmospheres in martensite

Once Cottrell atmospheres are formed around the dislocations, the probability of finding a solute atom in a lattice site i is not equal to the background concentration. In fact, there will be a concentration gradient around the dislocation that scales with the gradient of the interaction energy between the dislocation and the interstitials. For a dislocation positioned at the center of our reference system $(x_1,\ x_2 = 0)$ and dislocation line ξ along x_3, the probability of finding an interstitial at the position (x_1, x_2) in an OH site (that is, the local concentration of an OH site at (x_1, x_2)) can be estimated by using the Fermi-Dirac statistics [25,57,58]:

$$\frac{c(x_1,x_2)}{1-c(x_1,x_2)} = \frac{c_0}{1-c_0}\exp\left(\frac{E_b(x_1,x_2)}{k_B T}\right) \tag{20}$$

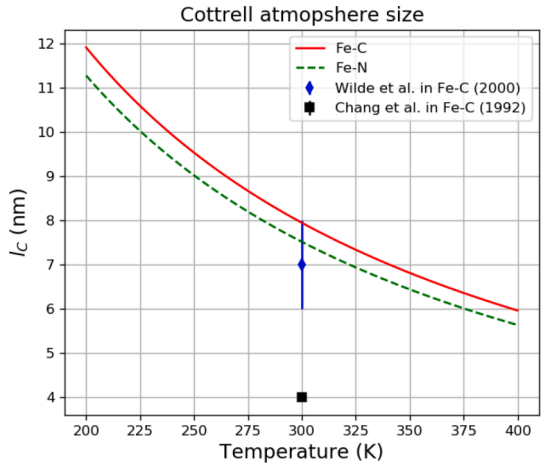

Fig. 6. Size of the Cottrell atmospheres as a function of temperature in Fe-C martensite, predicted by using Eq. (24) and compared against the available experimental measurements [21,64]. The error bars of ±1nm are included for the results of Wilde et al. [21]. (For interpretation of the references to colour in this figure legend, the reader is referred to the web version of this article.)

where $c_0 \ll 1$ is the background atomic fractional occupancy of an interstitial site and it is related to the background atomic fraction via $c_0 = c_0^{\text{af}}/3$; c_0^{af} with the factor 3 corresponding to three OH sites per one bcc lattice site. Even though c_0 represents the background concentration of interstitials far from the dislocation, in this case it can also be envisioned as the concentration of interstitials in one unit cell (see Fig. 5) since the size of Cottrell atmosphere l_c is much smaller than the average spacing between the dislocations $l = 1/\sqrt{\rho_d}$ (see below). Therefore, c_0 takes the same value in both Eqs. (18) and (20). The relationship between the atomic and weight concentration c_0^{wf} ("wf" stands for weight fraction) of interstitials can be expressed as $c_0^{\text{af}} = w\, c_0^{\text{wf}}$, where w is the weight factor which depends on the atomic weight of interstitials (e.g. $w \approx 4.526$ for C in Fe-C systems). $E_b(x_1, x_2)$ is the interaction energy between the dislocation and an interstitial atom, k_B is the Boltzmann constant and T is the temperature. Due to lattice periodicity along the dislocation line, the results computed using Eq. (20) can be inverted to determine the per-site equilibrium concentration

$$c(x_1, x_2) = \frac{c_0 \exp\left(\frac{E_b(x_1,x_2)}{k_B T}\right)}{1 + c_0 \exp\left(\frac{E_b(x_1,x_2)}{k_B T}\right)}. \tag{21}$$

For an OH site at the position (x_1, x_2) with respect to the dislocation core, Eq. (21) indicates a higher probability of being occupied than c_0 if $E_b(x_1, x_2) > 0$, and lower probability than c_0 if $E_b(x_1, x_2) < 0$.

Equation (21) holds if the C-C or N-N interactions are neglected. This is usually the case at distances sufficiently far from the dislocation core, where modest interaction energies between the dislocation and interstitials lead to a local concentration slightly larger than c_0. However, Eq. (21) is not valid close to the dislocation core; as a result of the large dislocation-interstitial interaction energies, the equation shows that all OH sites close to the dislocation would be ~ 100% saturated. Taking the interaction energy between C and a dislocation in α − Fe as an example ($E_b \approx 0.4$eV in the core computed using Fe-C potential [26]) and at a temperature $T = 300K$, Eq. (21) suggests that positive OH sites are 99.9% occupied within a distance $r = 2b$ from the dislocation core; in other words, there will be three C atoms per Fe atom within $r = 2b$. Such a concentration, which is 16 times higher than the concentration of C in cementite, is unrealistic and, to the best of the authors' knowledge, has never observed experimentally.

The C saturation concentration around both screw and edge dislocations was determined by Veiga and co-workers using a combination of Monte-Carlo and Molecular statics simulations [25]. Their results yield the saturation concentration of OH sites to be $c_d = 4\%$ and $c_d = 6\%$ around a screw and edge dislocation, respectively. Using this condition, Eq. (21) is modified to

$$c(x_1, x_2) = \begin{cases} \dfrac{c_0 \exp\left(\frac{E_b(x_1,x_2)}{k_B T}\right)}{1 + c_0 \exp\left(\frac{E_b(x_1,x_2)}{k_B T}\right)}, & \text{if } c(x_1, x_2) < c_d. \\ c_d, & \text{if } c(x_1, x_2) \geq c_d. \end{cases} \tag{22}$$

With the mapped interstitial concentration around the dislocation, see Eq. (22), the number of interstitial atoms trapped by the Cottrell atmosphere is

$$N_C = 3\frac{L}{\zeta}\sum_i c\left(x_1^i, x_2^i\right), \quad -l_C < x_1^i, x_2^i < l_C \tag{23}$$

where 3 is the number of OH sites per Fe site, L is the dislocation line length along x_3, l_C is the extent of a Cottrell atmosphere from the core, and ζ is the distance between atomic sites having the same (x_1, x_2); $\zeta = b$ for screw dislocations and $\zeta = 2\sqrt{2}b$ for edge dislocations. The size of l_C can be estimated using the same assumption as Cochardt and co-workers [20] in which the Cottrell atmosphere extends up to the point in which the dislocation-interstitial interaction energy is equilibrated by the thermal energy $k_B T$, i.e. $E_b = k_B T$.

Equation (22) and (23) clearly show that the interaction energy map $E_b = f(x_1, x_2)$ around a dislocation is of fundamental importance for the modeling of Cottrell atmospheres and the calculation of the number of atoms that they contain (N_C). Since the size of the Cottrell atmosphere is expected to extend significantly further than the core size, we deduce that $E_b = f(x_1, x_2)$ can be estimated using elasticity theory (see Eq. (17) and Appendix A). This final step will complete our analysis to enable the prediction of ρ_d *ab-initio*.

5.3. C and N misfit tensors

For the quantitative estimates of the model presented above (see Eqs. (19), (22) and (23)), we first calculate C and N misfit tensors by first principle methods. The results are presented in Table 1, while the calculation details are given in Appendix C. Comparing the entries of the two misfit tensors we find that C will lead to a slightly larger tetragonality compared to N, as it has been demonstrated experimentally [59]. We also note that the misfit volume $\Delta\Omega = \Omega_{ii}$ of N is slightly larger than that of C. However, this does not lead to a bigger strengthening effect of N since it is the tetragonal distortion which interacts with screw dislocations. The effects of N on the martensitic microstructure have been investigated by Morito and co-workers [15].

The DFT calculated C misfit volume is roughly two times larger than the one computed using a state of the art Fe-C EAM potential [26,60,61]. Since Becquart's potential was shown to reproduce well the interaction energies in the zones where the elasticity fails (the dislocation core), the difference found is expected to affect the long range interactions and it does not affect our estimates.

Furthermore, in addition to C and N misfit tensors, we use screw dislocation stress field for calculating the interaction energy. Using the screw dislocation stress field in Eq. (17) is a natural choice because the yield strength in martensite is controlled by the long screw dislocations which are aligned with the $< 111 >$ directions [62,63]. Dislocation stress field is estimated using anisotropic elasticity (see Appendix Appendix A) for which entries of the cubic stiffness tensor are computed using DFT ($C_{11} = 291.4$GPa, $C_{12} = 163.4$GPa and $C_{44} = 96.1$GPa). Finally, for all our calculations we rotate our crystal coordinates such that $x_1 = [1\ 2\ \bar{1}]$, $x_2 = [1\ 0\ 1]$ and $x_3 = [1\ \bar{1}\ \bar{1}]$ and position the dislocation at the origin $x_1 = x_2 = 0$ with line direction and Burgers vector aligned to x_3.

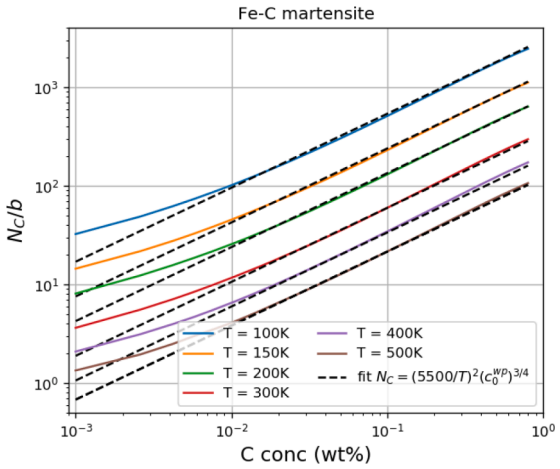

Fig. 7. Calculated number of C atoms within a Cottrell atmosphere around a screw dislocation in martensite as a function of the nominal concentration of C c_0^{wp} (wt%) and temperature (see Eq. (18)). The values calculated correspond to a dislocation length of $\zeta = b$. The black dashed line is a polynomial fit of the results computed using Eq. (23) . (For interpretation of the references to colour in this figure legend, the reader is referred to the web version of this article.)

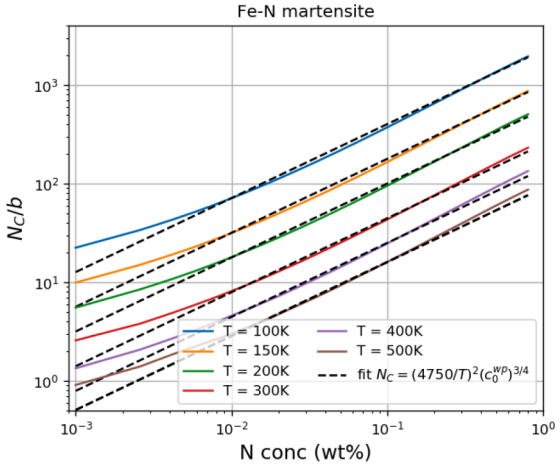

Fig. 8. Calculated number of N atoms within the Cottrell atmosphere around the screw dislocation in martensite as a function of the N nominal concentration c_0^{wp} (wt%) and temperature (see Eq. (18)). The values calculated correspond to the dislocation length of $\zeta = b$. The black dashed line is a polynomial fit of the results computed using Eq. (23). (For interpretation of the references to colour in this figure legend, the reader is referred to the web version of this article.)

6. Model validation

First, we assess the accuracy of the model prediction of the Cottrell atmospheres size l_C, which is computed as (see Eq. (A.14) and Section 5.2)

$$\sigma_{ij}^{d}(l_C)\Omega_{ij} = k_B T. \tag{24}$$

Results are shown in Fig. 6, for Fe-C and Fe-N martensite as a function of the temperature T, computed using Eq.(24) and the C/N misfit tensors (see Table 1). For both C and N, the size of $l_c = f(T)$ scales with $\sim 1/T$ due to the nature of the dislocation stress field. The predicted l_C is slightly larger in Fe-C than in Fe-N systems, because the predicted tetragonal distortion due to C is larger than the one due to N (see Table 1), and it is this distortion that interacts with the deviatoric stress field of the screw dislocation. The slightly larger volume misfit of N does not interact with the screw dislocation stress field and hence does not

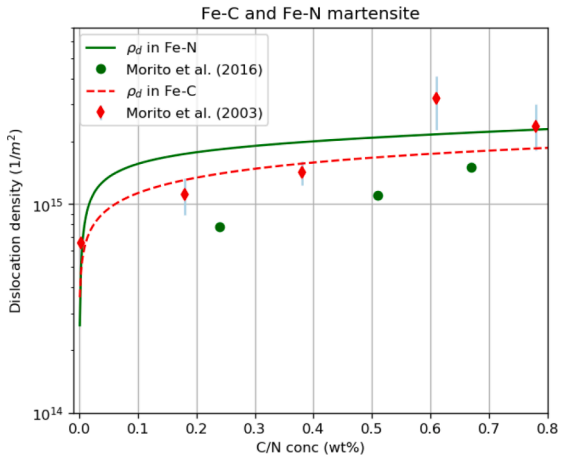

Fig. 9. Dislocation density ρ_d calculated using Eq. (19) at $T = 300$K as a function of the C and N concentrations in Fe-C and Fe-N martensite. The solid green and dashed red line correspond to N and C, respectively. Results are compared against the available experiments [15] (blue diamonds and green diamonds for N and C, respectively). (For interpretation of the references to colour in this figure legend, the reader is referred to the web version of this article.)

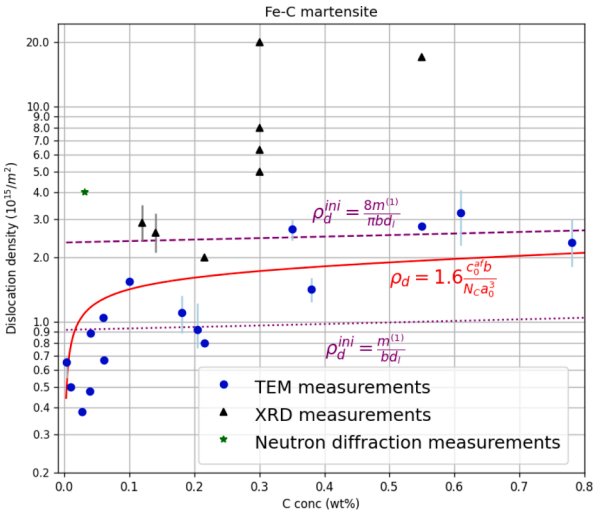

Fig. 10. Dislocation density in Fe-C martensite calculated using Eq. (19) (solid red line) versus experimental results measured using TEM [8–14] (blue circles), XRD [11,13,65–67] (black triangles), and neutron diffraction [68] (green star) experimental techniques. . (For interpretation of the references to colour in this figure legend, the reader is referred to the web version of this article.)

influence l_C. More importantly, the calculated value for l_C in Fe-C martensite at $T = 300K$ is $l_C = 8nm$, which falls within the experimental bounds of Wilde and collaborators ($l_C = 7 \pm 1nm$) [21].

The agreement between our predictions and experiments justifies the assumption that Cottrell atmospheres extend up to the point where the interstitial interaction energy is balanced by the thermal energy $k_B T$. However, our predictions are larger than earlier measurements by Chang et al. [64] which might be due to lower experimental accuracy, as pointed out by Wilde and co-workers [21]. Interestingly, our predictions are close to those by Cochardt et al. [20], in which the interaction energy between C and screw dislocation was estimate using the approximate value of the strain tensor of a $\alpha -$ Fe unit cell containing one C atom. The analysis presented here is more robust since the calculation of the interaction energy is based on Eshelby type analysis which is independent of the actual cell size in which an interstitial is inserted. To the best of our knowledge, there are no experimental results for l_C measured in

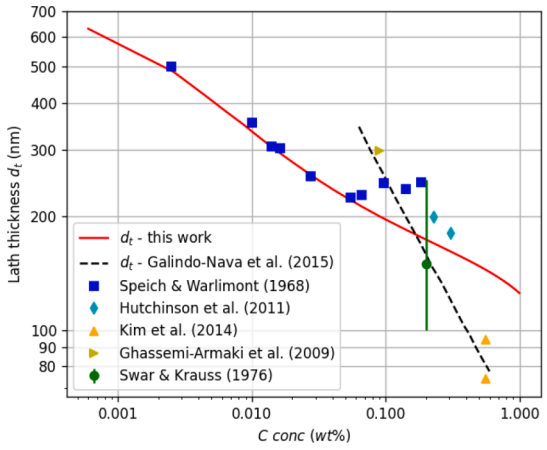

Fig. 11. Lath size d_t calculated using Eq. (27) (red solid line) at $T = 300$K as a function of the C concentration in Fe-C martensite. Results are compared against the available experimental results in Fe-C martensite [69,70,73] (blue squares, light blue diamonds and green circle, respectively). In addition, we compare our model to the recent model published by Galindo-Nava et al. [27] (black dashed line), and with the experimental results obtained in Si [71] and Cr [72] reach steels. (For interpretation of the references to colour in this figure legend, the reader is referred to the web version of this article.)

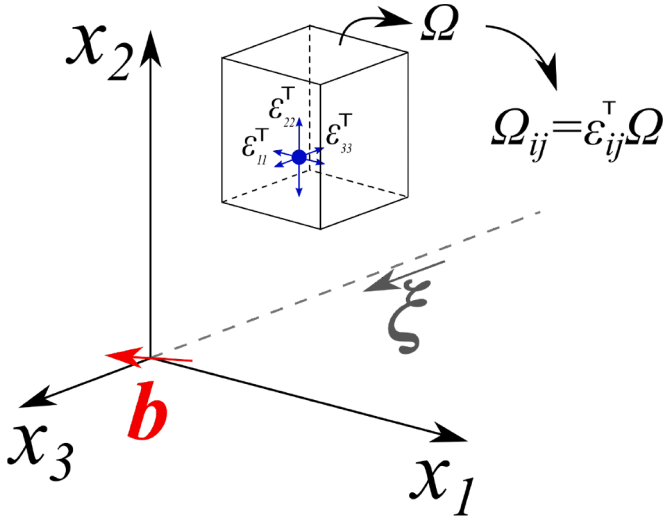

Fig. A1. A dislocation with burgers vector **b** and dislocation line ξ along x_3 axis in the vicinity of an interstitial solute (blue sphere) with identified associated eigenstrain tensor ε^T_{ij} within a volume Ω. The product $\Omega_{ij} = \varepsilon^T_{ij}\Omega$ is a well-defined physical quantity called misfit tensor which can be computed using first principle calculations (see Section Appendix C). (For interpretation of the references to colour in this figure legend, the reader is referred to the web version of this article.)

Table C1
Calculated stress and misfit tensors of the systems $Fe_{54}C$ and $Fe_{54}N$. Shear stresses are zero due to symmetry and are not shown here. The units of the stress tensors are in GPa, while the units of the misfit tensors are in Å^3.

	σ_{11}	σ_{22}	σ_{33}	Ω_{11}	Ω_{22}	Ω_{33}	$\Delta\Omega$
$Fe_{54}C$	-2.634	-2.634	-5.132	-0.55	-0.55	11.45	10.34
$Fe_{54}N$	-2.846	-2.846	-5.178	-0.13	-0.13	11.07	10.81

Fe-N martensite.

Next, we predict the number of C and N atoms trapped by a screw dislocation by using Eq. (23), as a function of the C/N nominal concentration c_0^{wp} (wt%) and temperature (wp = weight percent, wp = 100wf, wf = weight fraction). Limited experimental data, exclusively for Fe-C martensite, is available for model validation. By considering $c_0^{\text{ap}} = 0.85$ at $T = 300K$ in Eq. (23), there are 18 C atoms per [110] atomic layer along the dislocation line ($L = 4nm$). Again, our predictions are very close to the experimental results obtained by Wilde et al. who found 21 ± 1 C atom per [110] plane [21]. In addition, Chang et al. [64] measured 15 C atoms per [110] plane, again in good agreement with our predictions.

Figures 7 and 8 show that the number of C atoms trapped by a screw dislocation is slightly larger than the number of trapped N atoms. The reason is, again, the stronger screw dislocation-C interactions due to the larger tetragonal distortions in the misfit tensor. Furthermore, for both Fe-C and Fe-N, we find $N_C \sim (c_0^{\text{wp}})^{3/4}$ for $c_0^{\text{wp}} > 0.01$ wt%, and a slightly different behavior (smaller slope) for $c_0^{\text{wp}} < 0.01$ wt%. The change in the slope suggests that for a given temperature, N_C tends to converge to a particular value with reduction of the interstitial concentration. Such a behavior is a consequence of the very strong interaction close to the dislocation core which becomes dominant effect in N_C at very low C/N concentrations. The well defined dependency of N_C on the C/N nominal concentration for $c_0^{\text{wp}} > 0.01$ enabled us to derive two approximate solutions

$$N_C^C = \left(\frac{5500}{T}\cdot 1K\right)^2 (c_0^{\text{wp}})^{\frac{3}{4}}, \quad c_0^{\text{wp}} > 0.01\text{wt\%} \tag{25}$$

for Fe-C systems and,

$$N_C^N = \left(\frac{4750}{T}\cdot 1K\right)^2 (c_0^{\text{wp}})^{\frac{3}{4}}, \quad c_0^{\text{wp}} > 0.01\text{wt\%} \tag{26}$$

for Fe-N systems. In the above two equations, T is the absolute temperature in Kelvins and c_0^{wp} is the nominal concentration in wt%. While Eqs. (25) and (26) are approximate, they are fitted using the well defined full solution for N_C (see Section 5.2 and Eq. (23)). This is the third main result of this article. The $N_C = f(c_0)$ dependence is due to the long range interactions between the dislocation and interstitials. For instance, taking the C-screw dislocation interaction in Fe-0.1wt%C martensite at $T = 300$K, along with DFT-computed C misfit tensor (see Table 1), we find that the saturation concentration extends up to ~ 2.2nm from the core. Since the Cottrell atmosphere extends 8nm from the core, it is the long range interaction which controls the precise value of N_C.

Finally, we compare the predicted dislocation density ρ_d (Eq. (19)) with the available experimental measurements obtained using TEM. Comparison of the model with experimental results obtained using other techniques, such as XRD and neutron diffraction, is discussed in Section 7. Figure 3 shows the predicted dislocation density as a function of the C concentration at $T = 300$K, together with experiments from literature [8–14]. The model predictions are compatible with the experiments across a wide range of C concentrations. With increasing of C concentration, we observe that ρ_d calculated using Eq. (19) converges to the value of the initial dislocation density ρ_d^{ini} which depends on the magnitude of the shape deformation $m^{(1)}$ due to the transformation. Such a behavior is a consequence of the stronger dislocation strengthening by C in the solid solution which prevents the process of the dislocation annihilation (see Section 4). By using the approximate solution for N_C^C (Eq. (25)) in combination with Eq. (19), we find that $\rho_d \sim (c_0^{\text{wp}})^{1/4}$ for C/N concentrations above 0.01wt%. As a consequence, the new model for the estimation of the dislocation density captures the expected trend for ρ_d with increasing C concentration, including a rapid increase in ρ_d for small C concentrations $0.001 < C_0^{\text{wp}} < 0.02$ wt%, and curve flattening for C concentrations $C_0^{\text{wp}} > 0.02$ wt%. These predictions outperforms the recent model of Galindo-Nava et al. [27], which underestimates ρ_d at low C concentrations, and overestimates it

significantly at higher C concentrations. A possible origin for this discrepancy is the effect of dislocation-C interactions, which were not included explicitly in Ref. [27], while constituting a key ingredient of the present model. The model of Galindo-Nava et al. [27] yields $\rho_d \sim (c_0^{\text{wp}})^{4/3}$, which is not confirmed by experiments. Possible implications are discussed in the next Section.

The present model tends to be an upper bound for C concentrations up to $C_0^{\text{wp}} \approx 0.4$ wt%, as previously discussed. On the contrary, the model tends to be a lower bound for C concentrations $C_0^{\text{wp}} > 0.5$ wt%. This trend is most likely associated with the martensite change from lath to plate microstructure: additional effects that might appear above ~ 0.5wt%, that are not included in this model (e.g. twinning, much thinner laths/higher density of interfaces), might lead to larger dislocation densities. However, the model is still capable to provide a reasonable quantitative estimate within the experimental accuracy. This is the fourth main result of this article.

We compare the model predictions for both Fe-N and Fe-C martensite with available experimental data [15]. Note that due to limited available data on dislocation density in Fe-N martensite, and for the sake of experimental consistency, we compare our predictions with experimental results published by Morito and co-workers only [15] on both alloys. Figure 9 shows the calculated dislocation density at $T = 300K$ as a function of N and C concentrations (solid green and dashed red line, respectively). The predicted dislocation density in Fe-N martensite is larger than that in Fe-C martensite. This trend is the result of the smaller interaction energy between the screw dislocation and N, which then leads to the smaller N_C^N and therefore a larger dislocation density needed to trap all the N from the solid solution. This is, however, not reflected by experiments, which show, on the contrary, a slightly larger dislocation density in Fe-C martensite. While the experimental data are limited to one reference with no available error bars, a possible reason for the discrepancy might be due a slower diffusion of N which then enables additional dislocation annihilation prior to dislocation pinning by Cottrell atmospheres. Further clarification remains to be addressed in the future. The predictions are again an upper bound, and the model preserves the correct scaling of ρ_d with the N concentration.

7. Discussion and implications

The present model, which matches the experimental scaling, is based on the understanding that the initial large dislocation density in martensite is due to the shape deformation caused by the martensitic transformation. This shape deformation depends on the lattice parameter ratio $r = a_{fcc}/a_{bcc}$, which in turn depends weakly on the interstitials content for the concentration range of interest for lath martensite. The dependence of the dislocation density on the interstitial atoms concentration is caused by the large interaction energy between interstitial solutes and dislocations, which play a key role in the processes that lead to energy minimization of the dislocation structure during (auto-tempering) or after (room-temperature annealing) quenching. The high energy associated with a large initial dislocation density ρ_d^{ini} and the interstitial atoms trapped in solid solution will be relaxed by dislocation annihilation and formation of Cottrell atmospheres. Here, we assume that a local minimum is achieved in which the dislocation density $\rho_d = 1/l^2$ yields a dislocation structure that is fully saturated with the interstitial elements (C or N), trapped in Cottrell atmospheres. The statistics of solute concentration around the dislocation core is corrected to account solute-solute repulsion (see Section 5.2 and Eq. (22)). The number of interstitials trapped within the Cottrell atmospheres depends on the long range interactions between a dislocation stress field and an interstitial misfit tensor Ω_{ij}. We have then demonstrated that ρ_d is directly proportional to c_0 and inversely proportional to $N_C = f(c_0)$. This observation yields a well defined dependency of the dislocation density on the background concentration of interstitials, yielding the scaling $\rho_d \sim c_0^{1/4}$ which is observed experimentally both for Fe-C and Fe-N martensite. The model matches very closely the experimental measurements of the dislocation density in Fe-C, as a function of C concentration.

The present model has some important implications, that go beyond the prediction of the dislocation density. First, experimental measurement of dislocation density is an extremely challenging and time consuming process. Several different experimental techniques exist such as those based on line interception using TEM [8–14], X-ray diffraction (XRD) method [11,13,13,65–67], and neutron diffraction methods [68]. However, despite the fact that the dislocation density in Fe-C and Fe-N martensite is one of the most important contributions to its overall yield strength, there is still an open experimental debate about the accuracy of each method (e.g. see discussion in Ref. [67]). Figure 10 shows the calculated initial Eqs. (12) and (13) and final (Eq. (19)) dislocation density along with the experimental results obtained using TEM, XRD and neutron diffraction method. Comparing the experimental results for a range of C concentrations we find that both XRD and neutron diffraction methods usually show much higher dislocation densities than those measured using TEM. While this discrepancy has been commented in a number of previous publications (for example, see Refs. [11,45,67]), a clarification about the most reliable quantitative method is not provided. Using the model proposed here we find that for a range of C concentrations Eq. (19) matches very well the experimental measurements obtained using TEM. Since the model proposed here depends on several material properties calculated from first principles, we conclude that TEM-based measurements might be the most reliable ones for the quantitative estimation of the dislocation density in martensite. However, the authors are aware that more experimental work is needed for a definitive confirmation of this implication.

It is now well known that laths are the basic building blocks of the lath-martensite hierarchical microstructure [6]. Experiments show that the lath thickness d_t depends on the background interstitials concentration (e.g. C) [69–73]. Laths within a single block have a similar crystallographic orientation, and the boundary between them is close to twist character with an angle mismatch ranging between 1° and 5° [54]. Due to the approximately twist nature of the lath-lath boundaries, the lattice mismatch along the lath boundaries is accommodated by interface dislocations which are, most likely, of screw character [[2]]. In the case in which thin films of austenite are retained at lath boundaries [53], which is due to increased C content or due to boundaries among laths from different variants (blocks/packets), the lath/retained austenite interface structure is still composed of a network of screw dislocations [2]. We can then conjecture that the C and N segregation to the lath boundaries is again driven by the long range interactions between their misfit tensor and the interface dislocations. Since our model does not differentiate between the interface and in-lath screw dislocations, we deduce that there should be a correlation between the dislocation density and the lath thickness/width. Note that this correlation holds since (i) the final dislocation density (Eq. (19)) depends solely on the number of atoms trapped by Cottrell atmosphere and the background concentration of C, and (ii) the initial dislocation density (Eq. (12)) depends on the lath length d_l and not on the lath thickness d_t. Starting from the definition of dislocation density $\rho_d = N/d_l d_t$, and assuming that the lath length d_l and total number of dislocations N are constant yields

$$d_t = \frac{N}{d_l \rho_d(c_0, T)}. \tag{27}$$

Using the lath thickness $d_l = 2.5\mu$m as in the estimation for the initial dislocation density, and $N = 700$ which in this case is not derived but a fitting constant, and $T = 300K$, we calculate the lath thickness as a function of C concentration in Fe-C martensite. The assumed $N = const$ can be envisioned as the constant energy contribution due to stored dislocations within the lath area S. In other words, reduction of the dislocation density will be manifested by increase in the lath width while

the total energy will be kept constant. Again, this conclusion is physically sounds because average increase in the lath thickness due to reduction of dislocation density caused by 1 minute long tempering has been observed by Swarr and Krauss [73] (see Figs. 7 and 8 in ref. [73]). Our predictions on d_t are presented in Fig. 11 (red line) along with the experimental measurements and the recent model of Galindo-Nava and collaborators [27] (black dashed line). Our model shows an excellent agreement with the well defined, low-C content range of Speich and Warlimont [69], carried out in Fe-C lath martensite. Our model also compares to other experimental results carried out by Hutchinson et al. [70] and Swar and Krauss [73] in Fe-C martensite. The mismatch at higher C content might be due to gradual changes in morphology, that occur around 0.6 wt%, and to an increased role of secondary phases such as retained austenite and carbides - not considered in this model.

We now compare our model with the one derived by Galindo-Nava et al. [27] in which the lath thickness is calculated as $d_{lath} = l_C / (c_0^{\text{af}})^{2/3}$ with $l_C = 7$nm size of the Cottrell atmosphere (taken from the experiments), and c_0^{af} the atomic fraction of C. Figure 11 shows that the model in Ref. [27] does not capture the experimental trends in Fe-C. A possible reason for the discrepancy is the choice for the ad-hoc dependency of the lath size on C concentration. On the contrary, the model in Ref [27]. matches well the experiments by Kim et al. [71] and Ghassemi-Armaki et al. [72], contrarily to the present model. The discrepancy between the present model and experiments at larger C might be due to secondary phases, as mentioned earlier, and to the specific steel grades tested in these two experiments, which have very high Si (which is also a carbide retarder and hence could help retaining austenite) and Cr contents, respectively. In these cases, the effect of additional alloying elements needs to be taken into account.

The yield strength of Fe-C martensite is usually estimated using a semi-analytical microstructural model [1]

$$\sigma_y(0.2\%) = \sigma_{HP} + \sigma_C + \sigma_d \tag{28}$$

where σ_{HP} is the strengthening due to Hall-Petch effect, σ_C is the strengthening contribution due to interaction of C with the dislocations (C in solid solution and/or in Cottrell atmospheres), and $\sigma_d = \beta M \mu b \sqrt{\rho_d}$ is the strengthening contribution due to the dislocation density, where $\beta = 0.2 - 0.4$ is a scaling coefficient [74], and $M = 2.75$ is the Taylor factor for bcc materials [75]. The present analysis sheds light on the strengthening contribution due to dislocation density, as a function of C concentration. According to the present model, $\rho_d \sim c_0^{1/4}$ (see Eq. (19)). By using this relationship in the relation for σ_d, we find $\sigma_d \sim c_0^{1/8}$. Thus, after a rapid increase in σ_d with C ($c_0^{wp} < 0.01$), σ_d depends weakly on C $c_0^{wp} > 0.01$. This is a very interesting observation since it is known experimentally that the yield strength in low-C martensite scales as $\sigma_y(0.2\%) \sim c_0^{1/2}$. Therefore, we deduce that the observed martensite yield strength scaling with C is most likely controlled by strengthening of screw dislocations by Cottrell atmospheres. This is the topic of current research.

Several extensions of the model presented here are necessary. First, in the current model we do not consider the kinematic effects related to C/N diffusion nor the effect of alloying elements on their diffusivity [19,76]. It is expected, as Fig. 11 suggests, that alloying elements (e.g. with Si or Cr) affect C diffusion, the formation of dislocation substructures, and the dislocation density. Second, the current model suggests that ρ_d increases with increased T, since N_C decreases (see Eqs. (23) and (25)). However, this might not be the case for higher temperatures since the available thermal energy will lead to the annihilation of dislocations, cementite precipitation and, therefore, lower dislocation density. The current model is expected to be be valid for $T < 450K$ (low temperature tempering). Finally, the possible presence of interlath retained austenite films, which can play a key role in lath martensite plasticity [7,77], is not considered. C is expected to enrich these films. However, it has been shown that the retained austenite/lath interface consists of a network of screw dislocations [2] which can then be considered, as a first approximation, as a part of the overall martensite dislocation density, and that can be as well strengthened by C segregation.

8. Conclusions

An elasticity model based on the interaction between the stress field of dislocations and the misfit tensor of interstitial elements has been proposed for modeling the size of Cottrell atmospheres and the number of interstitials trapped by the atmosphere N_C. The misfit tensor of C and N is computed using first principle calculations. Using the results for N_C we have derived a closed-form expression for ρ_d, which scales as $\rho_d \sim c_0^{1/4}$ (with c_0 the C/N concentration). Two simplified closed form solutions for N_C and ρ_d were proposed. Finally, and most importantly, the current model sets a pathway towards a theory for predicting the strength of lath martensite as a function of the interstitial elements concentration. We will report on research examining these and other implications in the near future.

Declaration of Competing Interest

The authors declare that they have no known competing financial interests or personal relationships that could have appeared to influence the work reported in this paper.

Acknowledgments

This work was supported in part through the computational resources and staff contributions provided for the TulipX high performance computing facility at SKF Research & Technology Development, Houten, The Netherlands.

Appendix A. Interaction energy between dislocation and interstitials

A1. Dislocation stress field

According to linear elasticity, the components of the small strain tensor (ϵ_{ij}) are related to the components of the displacement field (u_i) by the compatibility condition $\epsilon_{ij} = (u_{i,j} + u_{j,i})/2$, where $(\cdot)_{,i}$ denotes partial differentiation with respect to the Cartesian directions x_i. The stress tensor itself relates to the strain tensor via the Hooke's law $\sigma_{ij} = C_{ijkl}\epsilon_{kl}$, where C_{ijkl} is the elastic stiffness tensor. Since our study deals with dislocations, which are line defects aligned with specific crystallographic directions in a crystal, we generalize the analysis at the outset to anisotropic elasticity. In fact, we calculate the anisotropic factor $A = 2C_{44}/(C_{11} - C_{12}) = 1.5$ in $\alpha-$ Fe where entries of the cubic stiffness tensor are computed using DFT ($C_{11} = 291.4$GPa, $C_{12} = 163.4$GPa and $C_{44} = 96.1$GPa). Therefore, isotropic elasticity is not applicable to our case since macroscopic isotropic elastic properties only emerge in polycrystalline aggregates [78].

We begin our analysis by inserting an infinitely long dislocation into an elastic anisotropic medium. The dislocation is inserted by making a cut on the $x_1 - x_3$ plane in the range $\infty < x_1 < 0$ (see Fig. A.12). The created dislocation is positioned at the origin $(x_1,\ x_2 = 0)$ with the dislocation line ξ along the x_3 axis. The displacement and stress fields need to satisfy the boundary conditions

$$u_i(x_1,\ +0) - u_i(x_1,\ -0) = \begin{cases} \mathbf{b}, & \text{for } x_1 > 0 \\ 0, & \text{for } x_1 \leq 0 \end{cases} \tag{A.1}$$

where $\mathbf{b} = [b_1,\ b_2,\ b_3]^T$ is the Burgers vector. In addition, there are no remote applied tractions. The solution of this boundary value problem is [79,80]

$$u_i = \frac{1}{\pi}\mathrm{Im}\{\mathbf{A} < f(z_\alpha) > \mathbf{D}^T\}\mathbf{b} \tag{A.2}$$

where $\mathbf{A} = [\mathbf{a_1}, \mathbf{a_2}, \mathbf{a_3}]$ and $\mathbf{D} = [\mathbf{d_1}, \mathbf{d_2}, \mathbf{d_3}]$ are complex-valued matrices composed of the eigenvectors $\mathbf{a_i}$ and $\mathbf{d_i}$. The angle bracket notation in Eq. (A.2) is used to represent the elements of a diagonal matrix in the following way:

$$< f(z_\alpha) >= \mathrm{diag}[f(z_1), f(z_2), f(z_3)] \tag{A.3}$$

where

$$f(z_\alpha) = \ln z_\alpha \tag{A.4a}$$

$$z_\alpha = x_1 + p_\alpha x_2 \tag{A.4b}$$

while $\mathbf{p} = p_\alpha$, $\mathbf{A}$ and $\mathbf{D}$ satisfy the following eigenvalue problem

$$\boldsymbol{N}\begin{bmatrix}\mathbf{A}\\ \mathbf{D}\end{bmatrix} = \boldsymbol{p}\begin{bmatrix}\mathbf{A}\\ \mathbf{D}\end{bmatrix}. \tag{A.5}$$

In the previous equations, $\mathbf{p} = \langle p_\alpha \rangle = \mathrm{diag}[p_\alpha]$ are the eigenvalues defined in the Stroh formalism [81,82], and $\mathbf{N}$ is the fundamental elasticity matrix computed from the stiffness tensor aligned with a particular crystallographic orientation [79]. See Appendix A.3 for a more detailed derivation of $\mathbf{N}$. The corresponding solution to the stress field is

$$[\sigma_{11}, \sigma_{21}, \sigma_{31}]^T = -\frac{1}{\pi}\mathrm{Im}\{\mathbf{D}\mathbf{p}\Lambda\mathbf{D}^T\}\mathbf{b} \tag{A.6a}$$

$$[\sigma_{12}, \sigma_{22}, \sigma_{32}]^T = \frac{1}{\pi}\mathrm{Im}\{\mathbf{D}\Lambda\mathbf{D}^T\}\mathbf{b} \tag{A.6b}$$

$$\sigma_{33} = -\frac{1}{S_{3333}}\sum_{i,j\neq 3} S_{33ij}\sigma_{ij}. \tag{A.6c}$$

where

$$\mathbf{p} = \mathrm{diag}[p_1, p_2, p_3] \tag{A.7a}$$

$$\mathbf{\Lambda} = \mathrm{diag}[1/z_1, 1/z_2, 1/z_3] \tag{A.7b}$$

In the limit $A \longrightarrow 1$, the above expression converges to the isotropic solution [52]. The elastic solution shown in Eqs. (A.2) and (A.6) is general and applies for a dislocation line along x_3, while the orientation of the stiffness tensor $\mathbb{C}$ and the Burgers vector $\mathbf{b} = [b_1, b_2, b_3]^T$ follow a particular slip plane/system.

Even though the above equations seem to be more complicated than their isotropic counterparts, their computation is straightforward by using standard programming libraries.[1] More importantly, the anisotropic medium does not change the well-known $1/x$ long-range nature of dislocation fields [31,83]. As already pointed out above in the text, the long range interactions are of crucial importance for an accurate description of the Cottrell atmospheres, and the calculation of ρ_d.

A2. Elastic stress field due to solutes and their interaction with dislocations

Solutes are point defects in a lattice. As such, they act as a source of elastic fields, and interact with external fields. We first consider the elastic fields generated by the insertion of a solute into an elastic medium. Even though the focus here is on interstitials (C and N), the analysis presented below is general and applies to both substitutional and interstitial solutes.

Inserting a solute into a lattice site generates local changes in the electron density, inducing self-equilibrating distortions around it. Since these lattice distortions result from chemically driven inelastic displacements, these can be analyzed by using Eshelby's inclusion method [83–85]. Here, the solute is treated as an inclusion having a volume Ω and undergoing an eigenstrain ε^T_{ij}. Assuming that there are no remote applied tractions, the displacement and stress fields at a point $\mathbf{x}$ of the linear elastic medium can be computed by means of the Green's function G_{ij} and its derivatives [31,79,86]

$$u_i(\mathbf{x}) = -G_{ij,k}(\mathbf{x})C_{jklm}\varepsilon^T_{lm}\Omega \tag{A.8a}$$

$$\sigma_{ij}(\mathbf{x}) = C_{ijkl}u_{k,l} = C_{ijkl}G_{lp,kq}C_{pqrs}\varepsilon^T_{rs}\Omega \tag{A.8b}$$

[1] A Python implementation can be provided on request to the corresponding author.

The closed-form expressions for the isotropic and anisotropic Green's function are provided in the Appendix A.4 for the plane strain case. Ω is the volume around the solute undergoing the eigenstrain ε_{ij}^{T}, after full relaxation. Even though the physical size of Ω is arbitrary, $\Omega_{ij} = \varepsilon_{ij}^{T}\Omega$ is a well-defined physical quantity, called misfit tensor, and can be expressed as a second rank tensor such that $\Omega_{ii} = \Delta\Omega$ is the *misfit volume* or *relaxation volume*. The properties of the misfit tensor depend on the type of alloying element (substitutional or interstitial solute). Due to symmetry considerations, Ω_{ij} is isotropic for substitutional solutes, while for interstitials it is anisotropic and associated to tetragonal lattice distortions.

We now consider the elastic interaction between a solute and an external stress field. The source of the external stress field can be of any kind (e.g. dislocations, cracks, external forces, etc.) and the exact origin is irrelevant for the analysis. We follow the standard analysis [31,83–85] and consider a body occupying a volume V with no alloying elements, subject to external tractions $\boldsymbol{T}^{A}$ applied over its boundary S. The enthalpy of the body is given by

$$H_1 = \frac{1}{2}\int_V \sigma_{ij}{}^{A}\epsilon_{ij}{}^{A}dV - \int_S T_i{}^{A}u_i{}^{A}dS \tag{A.9}$$

where $\sigma_{ij}{}^{A}$, $\epsilon_{ij}{}^{A}$ and $u_i{}^{A}$ are the stress, strain, and displacement fields due to the applied tractions T_i^{A}. The first term of the equation corresponds to the elastic energy stored in the volume V, and the second term is the work done by the applied tractions $T_i{}^{A}$ on S. We now consider the insertion of an alloying element, represented as an inclusion of volume Ω having the same elastic modulus as the surrounding material, and undergoing an eigenstrain ϵ_{ij}^{T} due to local changes in the electron density. The enthalpy of the second system is

$$\begin{aligned} H_2 \quad &= \frac{1}{2}\int_V \left(\sigma_{ij}{}^{A} + \sigma_{ij}\right)\left(\epsilon_{ij}{}^{A} + \epsilon_{ij} - \epsilon_{ij}{}^{T}\right)dV \\ &- \int_S T_i{}^{A}\left(u_i{}^{A} + u_i\right)dS + \Psi \end{aligned} \tag{A.10}$$

where σ_{ij}, $\epsilon_{ij} - \epsilon_{ij}{}^{T}$ and u_i are the *unknown* stress, *elastic* strain and displacement fields, respectively, generated by the inclusion that undergoes the eigenstrain $\boldsymbol{\epsilon}^{T}$. In addition, Ψ represents the inelastic (chemical) contribution of the solute to the total energy. Equation (A.10) can be rearranged using integration by parts and Gauss' theorem, yielding

$$\begin{aligned} H_2 \quad &= \frac{1}{2}\int_V \sigma_{ij}{}^{A}\epsilon_{ij}{}^{A}dV - \int_S T_i{}^{A}u_i{}^{A}dS \\ &- \frac{1}{2}\int_\Omega \sigma_{ij}\epsilon_{ij}{}^{T}d\Omega - \int_\Omega \sigma_{ij}{}^{A}\varepsilon_{ij}{}^{T}d\Omega + \Psi. \end{aligned} \tag{A.11}$$

Since the eigenstrain $\varepsilon_{ij}{}^{T}$ is constant inside the volume Ω, and $\varepsilon_{ij}{}^{T}\Omega = \Omega_{ij}$ is a well-defined physical quantity (misfit tensor), Eq. (A.11) can be further simplified to

$$\begin{aligned} H_2 \quad &= \frac{1}{2}\int_V \sigma_{ij}{}^{A}\epsilon_{ij}{}^{A}dV - \int_S T_i{}^{A}u_i{}^{A}dS \\ &- \frac{1}{2}\sigma_{ij}\Omega_{ij} - \sigma_{ij}{}^{A}\Omega_{ij} + \Psi. \end{aligned} \tag{A.12}$$

The enthalpy change under the action of an external stress of a solute atom inserted in the lattice is

$$\Delta H = H_2 - H_1 = -\frac{1}{2}\sigma_{ij}\Omega_{ij} - \sigma_{ij}{}^{A}\Omega_{ij} + \Psi \tag{A.13}$$

where the first term is the contribution to the elastic energy due to the solute itself, the second term is the *interaction energy* between the solute's misfit and the external applied stress. When a dislocation is the source of the external stress field σ_{ij}^{d} (see Eq. (A.6)), the interaction energy is

$$E_b = -\sigma_{ij}^{d}\Omega_{ij} \tag{A.14}$$

where both the stress tensor and the misfit tensor are expressed with respect to the same coordinate system. From a thermodynamic point of view, for a solute atom sitting at a position (x_1, x_2) with respect to the dislocation core, a positive interaction energy indicates a reduction in the total energy compared to the system in which the solute is far from the dislocation. Note, that the above expression can be simplified in the case of a substitutional solute (e.g. Si in $\alpha-$ Fe), leading to

$$E_b = p_h\Delta\Omega \tag{A.15}$$

in which $p_h = \frac{1}{3}\sigma_{ii}$ is the hydrostatic pressure due to the presence of a dislocation. With the known elastic properties of the Fe bcc lattice, and the interstitial misfit tensors computed ab-initio (see Section Appendix C), the set of equations (19), (23) and (A.14) is sufficient for the calculation of the dislocation density in martensite as a function of the interstitials concentration and temperature.

A3. Fundamental elasticity matrix

As pointed out in the main text, the solution for the dislocation stress and displacement field needs to satisfy the following eigenvalue equation

$$\boldsymbol{N}\begin{bmatrix}\mathbf{A}\\ \mathbf{D}\end{bmatrix} = \boldsymbol{p}\begin{bmatrix}\mathbf{A}\\ \mathbf{D}\end{bmatrix} \tag{A.16}$$

where $\mathbf{N}$ is the *fundamental elasticity matrix* [87] defined as

$$\mathbf{N} = \begin{bmatrix}\mathbf{N}_1 & \mathbf{N}_2\\ \mathbf{N}_3 & \mathbf{N}_1^T\end{bmatrix} \tag{A.17}$$

with

$$\boldsymbol{N}_1 = -\boldsymbol{T}^{-1}\boldsymbol{R}^{\boldsymbol{T}}, \tag{A.18a}$$

$$\boldsymbol{N}_2 = \boldsymbol{T}^{-1}, \tag{A.18b}$$

$$\boldsymbol{N}_3 = \boldsymbol{R}\boldsymbol{T}^{-1}\boldsymbol{R}^{\boldsymbol{T}} - \boldsymbol{Q} \tag{A.18c}$$

and

$$\boldsymbol{Q} = \begin{bmatrix}C_{11} & C_{16} & C_{15}\\ C_{16} & C_{66} & C_{56}\\ C_{15} & C_{56} & C_{55}\end{bmatrix}, \tag{A.19a}$$

$$\boldsymbol{R} = \begin{bmatrix}C_{16} & C_{12} & C_{14}\\ C_{66} & C_{26} & C_{46}\\ C_{56} & C_{25} & C_{45}\end{bmatrix}, \tag{A.19b}$$

$$\boldsymbol{T} = \begin{bmatrix}C_{66} & C_{26} & C_{46}\\ C_{26} & C_{22} & C_{24}\\ C_{46} & C_{24} & C_{44}\end{bmatrix}. \tag{A.19c}$$

C_{ij} in Eq. (A.19) are the components of the material stiffness tensor written in contracted (Voigt) notation.

Complex matrices $\mathbf{A} = [\mathbf{a_1}, \mathbf{a_2}, \mathbf{a_3}]$ and $\mathbf{D} = [\mathbf{d_1}, \mathbf{d_2}, \mathbf{d_3}]$ are composed of eigenvectors $\mathbf{a}$ and $\mathbf{d}$, respectively, which are normalized such that

$$\mathbf{d}_\alpha^T\mathbf{a}_\beta + \mathbf{a}_\alpha^T\mathbf{d}_\beta = \delta_{\alpha\beta} \tag{A.20}$$

where $\delta_{\alpha\beta}$ is Kronecker delta.

The second rank Stroh tensor with anisotropic energy coefficients is calculated as

$$\boldsymbol{H} = \frac{1}{2}\mathrm{Re}\left(\mathrm{i}\mathbf{A}\mathbf{D}^{-1}\right) \tag{A.21}$$

A4. Green's function in elastic medium

Green's function represents the displacement in direction i caused by a point force at $\mathbf{x} = 0$ in direction m. For an isotopic material it can be expressed as

$$g_{im} = \frac{1}{16\pi(1-\nu)\mu}\left[(3-4\nu)\frac{\delta_{im}}{X} + \frac{x_i x_m}{X^3}\right] \tag{A.22}$$

where μ and ν are the shear modulus and Poisson's ratio, respectively, δ_{ij} is Kronecker delta, and $X = \sqrt{x_1^2 + x_2^2 + x_3^2}$ is the absolute distance between the point force and point of interest at a position $\mathbf{x}$. The corresponding first and second derivatives of the Green's function are

$$\begin{aligned} g_{im,n} = \; & \frac{1}{16\pi(1-\nu)\mu}\Bigg[-(3-4\nu)\delta_{im}\frac{x_n}{X^3} \\ & -3\frac{x_i x_m x_n}{X^5} + \frac{\delta_{mn}x_i}{X^3} + \frac{\delta_{in}x_m}{X^3}\Bigg] \end{aligned} \tag{A.23}$$

and

$$g_{im,nl} = \frac{1}{16\pi(1-\nu)\mu X^3}\Big[(3-4\nu)(3q_nq_l\delta_{im}-\delta_{im}\delta_{nl}) - 3(q_mq_n\delta_{il}+q_iq_n\delta_{ml}+q_iq_m\delta_{nl}-5q_iq_mq_nq_l) - 3(q_iq_l+q_mq_l)+\delta_{mn}\delta_{il}+\delta_{in}\delta_{lm}\Big] \tag{A.24}$$

respectively, where $q_i = \frac{x_i}{X}$. In anisotropic elasticity, there is no closed form solution for 3D space. However, an elegant solution exists for 2D plane strain approximation (line force along x_3) and it can be expressed as [82]:

$$u_i = \frac{1}{\pi}\mathrm{Im}\{\mathbf{A}<f(z_\alpha)>\mathbf{A}^T\}\mathbf{f} \tag{A.25}$$

for a displacement field and

$$[\sigma_{11},\sigma_{21},\sigma_{31}]^T = -\frac{1}{\pi}\mathrm{Im}\{\mathbf{DP}\Lambda\mathbf{A}^T\}\mathbf{f} \tag{A.26a}$$

$$[\sigma_{12},\sigma_{22},\sigma_{32}]^T = \frac{1}{\pi}\mathrm{Im}\{\mathbf{D}\Lambda\mathbf{A}^T\}\mathbf{f} \tag{A.26b}$$

$$\sigma_{33} = -\frac{1}{S_{3333}}\sum_{i,j\neq 3} S_{33ij}\sigma_{ij} \tag{A.26c}$$

for a stress field, where $\mathbf{f} = [f_1, f_2, f_3]^T$ is the array of line forces along x_3.

Appendix B. Simulation of screw dislocation network along lath boundary

We create a junction network by rotating two halves of a Bulk Fe supercell around the [110] axis by an appropriate twist angle (see Fig. 1d). We consider a twist rotation angle of 5.4° corresponding to a Σ451 grain boundary. Low angle twin grain boundaries, such as the one that we generated, are equivalent to networks of screw dislocations [88]. It has also been seen experimentally that the misorientation between lath boundaries is usually low [54,89]. The system is generated using the software aimsGB [90] and ASE [91], and its energy is minimized using the software LAMMPS [92] with the interatomic potential developed in [93]. The interface structure is visualized and analyzed using OVITO dislocation analysis (DXA) [94–96].

Appendix C. C and N misfit tensors: DFT calculations

All the calculations were done using Density functional theory (DFT) [97,98] and the Projector Augmented Wave (PAW) method [99–101] as implemented in the software ABINIT [102]. The Perdew-Burke-Ernzerhof [103] Generalised Gradient Approximation (PBE-GGA [104–107]) functional was used. Pulay mixing of the density based on the seven previous iterations was used for the Self-Consistent-Field (SCF) cycle. A tolerance for the potential residual of 1.0×10^{-10} was used for the convergence of the SCF cycle, while the tolerance for the convergence of the forces for structural optimizations was set to $5\times10^{-5}E_h a_0^{-1}$. We used spin-polarized (collinear) calculations with separate and different wave functions for up and down spin electrons for each band and k point. A uniform grid of $6\times6\times6$ was employed, resulting in a total of 108 k-points. 520 bands and a cut-off energy of $20E_h$ were used.

A supercell containing exclusively Fe atoms arranged in a bcc structure in a periodic orthogonal box was generated using the software ASE [91]. The system contains three bcc unit cells on each direction for a total of 54 Fe atoms. We will refer to this system as Fe_{54}. Successive relaxations of the positions of the atoms and the cell geometry, using the algorithms fast inertial relaxation engine (FIRE) [108] and Broyden-Fletcher-Goldfarb-Shanno (BFGS) were applied to the system to ensure equilibrium [109]. The lattice constant converged to 2.835Å consistent with other experimental and calculated values found in the literature [110–115].

The relaxed reference system was used as the base for the generation of two supplementary configurations containing an additional interstitial atom (C or N) in an octahedral position. We will refer to these two systems as $Fe_{54}C$ and $Fe_{54}N$. The coordinates of the atoms of the newly generated systems were relaxed via the same procedure used previously for the reference system, but maintaining the volume of the box fixed. After relaxation of the atomic positions of the $Fe_{54}C$ and $Fe_{54}N$ systems, the stress tensor σ_{ij} was extracted. The results are presented in Table C.2.

Using the $\alpha-Fe$ DFT simulated stress tensor ($C_{11}=291.4$GPa, $C_{12}=163.4$GPa and $C_{44}=96.1$GPa) we calculate the misfit tensor as [86]

$$\Omega_{ij} = -S_{ijkl}\sigma_{kl}V \tag{C.1}$$

where S_{ijkl} is the bcc $\alpha-$Fe compliance tensor and V is the volume of the system Fe_{54}. Note that S_{ijkl} and σ_{ij} are both expressed in the cubic coordinate system. The solution to Eq. (C.1) is presented in Table 1.

References

[1] H. Bhadeshia, R. Honeycombe, Steels: Microstructure and Properties, Butterworth-Heinemann, 2017.

[2] F. Maresca, W. Curtin, The austenite/lath martensite interface in steels: structure, athermal motion, and in-situ transformation strain revealed by simulation and theory, Acta Mater. 134 (2017) 302–323.

[3] E. Clouet, L. Ventelon, F. Willaime, Dislocation core field. II. Screw dislocation in iron, Phys. Rev. B Condensed Matter Mater.Phys. 84 (22) (2011) 1–12, https://doi.org/10.1103/PhysRevB.84.224107.

[4] G.A. Nematollahi, J. von Pezold, J. Neugebauer, D. Raabe, Thermodynamics of carbon solubility in ferrite and vacancy formation in cementite in strained pearlite, Acta Mater. 61 (5) (2013) 1773–1784, https://doi.org/10.1016/j.actamat.2012.12.001.

[5] F. Maresca, E. Polatidis, M. Šmíd, H. Van Swygenhoven, W.A. Curtin, Measurement and prediction of the transformation strain that controls ductility and toughness in advanced steels, Acta Mater. 200 (2020) 246–255.
[6] S. Morito, H. Tanaka, R. Konishi, T. Furuhara, T. Maki, The morphology and crystallography of lath martensite in Fe-C alloys, Acta Mater. 51 (6) (2003) 1789–1799.
[7] F. Maresca, V. Kouznetsova, M. Geers, W. Curtin, Contribution of austenite-martensite transformation to deformability of advanced high strength steels: from atomistic mechanisms to microstructural response, Acta Mater. 156 (2018) 463–478.
[8] M. Kehoe, P. Kelly, The role of carbon in the strength of ferrous martensite, Scr. Metall. 4 (6) (1970) 473–476, https://doi.org/10.1016/0036-9748(70)90088-8.
[9] L.-Å. Norström, The relation between microstructure and yield strength in tempered low-carbon lath martensite with 5% nickel, Metal Sci. 10 (12) (1976) 429–436.
[10] S. Morito, J. Nishikawa, T. Maki, Dislocation density within lath martensite in Fe-C and Fe-Ni alloys, ISIJ Int. 43 (9) (2003) 1475–1477.
[11] J. Macchi, S. Gaudez, G. Geandier, J. Teixeira, S. Denis, F. Bonnet, S.Y. Allain, Dislocation densities in a low-carbon steel during martensite transformation determined by in situ high energy X-ray diffraction, Mater. Sci. Eng. A 800 (2021) 140249.
[12] J. Pešička, R. Kužel, A. Dronhofer, G. Eggeler, The evolution of dislocation density during heat treatment and creep of tempered martensite ferritic steels, Acta Mater. 51 (16) (2003) 4847–4862.
[13] T. Masumura, K. Inami, K. Matsuda, T. Tsuchiyama, S. Nanba, A. Kitahara, Quantitative evaluation of dislocation density in as-quenched martensite with tetragonality by X-ray line profile analysis in a medium-carbon steel, Acta Mater. (2022) 118052.
[14] T. Furuhara, K. Kobayashi, T. Maki, Control of cementite precipitation in lath martensite by rapid heating and tempering, ISIJ Int. 44 (11) (2004) 1937–1944.
[15] S. Morito, Y. Iwami, T. Koyano, T. Ohba, Effect of solution carbon and nitrogen on the microstructural size and crystallography of lath martensite in Fe–N and Fe–C alloys, Mater. Trans. 57 (3) (2016) 227–232.
[16] S. Echeverri Restrepo, S.W. Ooi, P. Yan, P. Andric, R.H. Vegter, J. Lai, Dark etching regions under rolling contact fatigue: a review, Mater. Sci. Technol. 37 (4) (2021) 347–376, https://doi.org/10.1080/02670836.2021.1916252.
[17] A.H. Cottrell, B.A. Bilby, Dislocation theory of yielding and strain ageing of iron, Proc. Phys. Soc. London Sect. A 62 (1) (1949) 49–62, https://doi.org/10.1088/0370-1298/62/1/308.
[18] G.A. Nematollahi, B. Grabowski, D. Raabe, J. Neugebauer, Multiscale description of carbon-supersaturated ferrite in severely drawn pearlitic wires, Acta Mater. 111 (2016) 321–334.
[19] S.E. Restrepo, P. Andric, A.T. Paxton, Effect of crystal defects in iron on carbon diffusivity: analytical model married to atomistics, Phys. Rev. Mater. 6 (10) (2022) L100801.
[20] A. Cochardt, G. Schoek, H. Wiedersich, Interaction between dislocations and interstitial atoms in body-centered cubic metals, Acta Metall. 3 (6) (1955) 533–537.
[21] J. Wilde, A. Cerezo, G. Smith, Three-dimensional atomic-scale mapping of a Cottrell atmosphere around a dislocation in iron, Scr. Mater. 43 (1) (2000) 39–48.
[22] R. Chang, An atomistic study of fracture, Int. J. Fract. Mech. 6 (2) (1970) 111–125.
[23] X. Zhang, H. Wang, T. Hickel, J. Rogal, Y. Li, J. Neugebauer, Mechanism of collective interstitial ordering in Fe–C alloys, Nat. Mater. 19 (8) (2020) 849–854.
[24] G. Da Rosa, P. Maugis, J. Drillet, V. Hebert, K. Hoummada, Co-segregation of boron and carbon atoms at dislocations in steel, J. Alloys Compd. 724 (2017) 1143–1148.
[25] R.G. Veiga, M. Perez, C. Becquart, C. Domain, Atomistic modeling of carbon Cottrell atmospheres in bcc iron, J. Phys. Condens. Matter 25 (2) (2012) 025401.
[26] C. Becquart, J. Raulot, G. Bencteux, C. Domain, M. Perez, S. Garruchet, H. Nguyen, Atomistic modeling of an Fe system with a small concentration of C, Comput. Mater. Sci 40 (1) (2007) 119–129, https://doi.org/10.1016/j.commatsci.2006.11.005.
[27] E. Galindo-Nava, P. Rivera-Díaz-del Castillo, A model for the microstructure behaviour and strength evolution in lath martensite, Acta Mater. 98 (2015) 81–93.
[28] M. NI, Some Basic Problems of the Mathematical Theory of Elasticity, Springer Science and Business Media, 2013.
[29] A. Head, N. Louat, The distribution of dislocations in linear arrays, Aust. J. Phys. 8 (1) (1955) 1–7.
[30] J. Eshelby, F. Frank, F. Nabarro, XLI. The equilibrium of linear arrays of dislocations, London Edinb. Dublin Philos. Mag. J. Sci. 42 (327) (1951) 351–364.
[31] T. Mura, Micromechanics of Defects in Solids, Springer Science & Business Media, 2013.
[32] G.P.M. Leyson, W.A. Curtin, L.G. Hector, C.F. Woodward, Quantitative prediction of solute strengthening in aluminium alloys, Nat. Mater. 9 (9) (2010) 750–755.
[33] C. Varvenne, A. Luque, W.A. Curtin, Theory of strengthening in fcc high entropy alloys, Acta Mater. 118 (2016) 164–176.
[34] F. Maresca, W.A. Curtin, Mechanistic origin of high strength in refractory bcc high entropy alloys up to 1900k, Acta Mater. 182 (2020) 235–249.
[35] J. Song, W. Curtin, Atomic mechanism and prediction of hydrogen embrittlement in iron, Nat. Mater. 12 (2) (2013) 145–151.
[36] X. Zhou, A. Tehranchi, W.A. Curtin, Mechanism and prediction of hydrogen embrittlement in fcc stainless steels and high entropy alloys, Phys. Rev. Lett. 127 (17) (2021) 175501.
[37] H. Haftbaradaran, J. Song, W. Curtin, H. Gao, Continuum and atomistic models of strongly coupled diffusion, stress, and solute concentration, J. Power Sources 196 (1) (2011) 361–370.
[38] E. Clouet, S. Garruchet, H. Nguyen, M. Perez, C.S. Becquart, Dislocation interaction with C in α-fe: acomparison between atomic simulations and elasticity theory, Acta Mater. 56 (14) (2008) 3450–3460.
[39] P. Kelly, A. Jostsons, R. Blake, The orientation relationship between lath martensite and austenite in low carbon, low alloy steels, Acta Metall. Mater. 38 (6) (1990) 1075–1081.
[40] M. Onink, C. Brakman, F. Tichelaar, E. Mittemeijer, S. Van der Zwaag, J. Root, N. Konyer, The lattice parameters of austenite and ferrite in Fe-C alloys as functions of carbon concentration and temperature, Scr. Metall. Mater. (United States) 29 (8) (1993).
[41] J.-O. Andersson, T. Helander, L. Höglund, P. Shi, B. Sundman, Thermo-Calc & DICTRA, computational tools for materials science, Calphad 26 (2) (2002) 273–312.
[42] S. Morito, X. Huang, T. Furuhara, T. Maki, N. Hansen, The morphology and crystallography of lath martensite in alloy steels, Acta Mater. 54 (19) (2006) 5323–5331.
[43] B. Sandvik, C. Wayman, Characteristics of lath martensite: Part I. Crystallographic and substructural features, Metall. Trans. A 14 (4) (1983) 809–822.
[44] D. Saha, E. Biro, A. Gerlich, Y. Zhou, Effects of tempering mode on the structural changes of martensite, Mater. Sci. Eng. A 673 (2016) 467–475.
[45] B. Hutchinson, P. Bate, D. Lindell, A. Malik, M. Barnett, P. Lynch, Plastic yielding in lath martensites–an alternative viewpoint, Acta Mater. 152 (2018) 239–247.
[46] É. Ódor, B. Jóni, G. Ribárik, N.Q. Chinh, T. Ungár, P.J. Szabó, Deformation induced soft and hard lath packets enhance ductility in martensitic steels, Crystals 10 (5) (2020) 373.
[47] T. Ungár, S. Harjo, T. Kawasaki, Y. Tomota, G. Ribárik, Z. Shi, Composite behavior of lath martensite steels induced by plastic strain, a new paradigm for the elastic-plastic response of martensitic steels, Metall. Mater. Trans. A 48 (1) (2017) 159–167.
[48] J. Pešička, A. Aghajani, C. Somsen, A. Hartmaier, G. Eggeler, How dislocation substructures evolve during long-term creep of a 12% Cr tempered martensitic ferritic steel, Scr. Mater. 62 (6) (2010) 353–356.
[49] T. Schneider, E. Stoll, Molecular-dynamics study of a three-dimensional one-component model for distortive phase transitions, Phys. Rev. B 17 (3) (1978) 1302–1322, https://doi.org/10.1103/PhysRevB.17.1302.
[50] B. DÜNWEG, W. PAUL, Brownian dynamics simulations without Gaussian random numbers, Int. J. Mod. Phys. C 02 (03) (1991) 817–827, https://doi.org/10.1142/S0129183191001037.
[51] H. Bhadeshia, Driving force for martensitic transformation in steels, Metal Sci. 15 (4) (1981) 175–177.
[52] J. Hirth, J. Lothe, Theory of Dislocations, second ed., 1982.
[53] B. Sandvik, C. Wayman, Crystallography and substructure of lath martensite formed in carbon steels, Metallography 16 (2) (1983) 199–227.
[54] A.H. Pham, T. Ohba, S. Morito, H. Taisuke, Energetic stability of boundary between variants in lath martensite, J. Alloys Compd. 577 (2013) S583–S586.
[55] V.V. Bulatov, W. Cai, Nodal effects in dislocation mobility, Phys. Rev. Lett. 89 (11) (2002) 9–12, https://doi.org/10.1103/PhysRevLett.89.115501.
[56] E. Tochigi, A. Nakamura, N. Shibata, Y. Ikuhara, Dislocation structures in low-angle grain boundaries of α-Al2O3, Crystals 8 (3) (2018) 133, https://doi.org/10.3390/cryst8030133.
[57] N. Louat, The effect of temperature on Cottrell atmospheres, Proc. Phys. Soc. London Sect. B 69 (4) (1956) 459.
[58] D. Beshers, On the distribution of impurity atoms in the stress field of a dislocation, Acta Metall. 6 (8) (1958) 521–523.
[59] O.D. Sherby, J. Wadsworth, D.R. Lesuer, C.K. Syn, Revisiting the structure of martensite in iron-carbon steels, Mater. Trans. 49 (9) (2008) 2016–2027.
[60] C. Becquart, J.-M. Raulot, G. Bencteux, C. Domain, M. Perez, S. Garruchet, H. Nguyen, Atomistic modeling of an fe system with a small concentration of C, Comput. Mater. Sci 40 (1) (2007) 119–129.
[61] R.G. Veiga, M. Perez, C. Becquart, E. Clouet, C. Domain, Comparison of atomistic and elasticity approaches for carbon diffusion near line defects in α-iron, Acta Mater. 59 (18) (2011) 6963–6974.
[62] F.R.N. Nabarro, Z.S. Basinski, D. Holt, The plasticity of pure single crystals, Adv. Phys. 13 (50) (1964) 193–323.
[63] F. Maresca, W.A. Curtin, Theory of screw dislocation strengthening in random bcc alloys from dilute to æhigh-entropyg alloys, Acta Mater. 182 (2020) 144–162.
[64] G. Krauss, P.E. Repas, Gilbert R. Speich Symposium Proceedings: Fundamentals of Aging and Tempering in Bainitic and Martensitic Steel Products: An International Symposium Held at the 34th Mechanical Working and Steel Processing Conference: Montreal, Quebec, Canada: October 25–28, 1992, Iron and Steel Society, 1992.
[65] T. Vershinina, M. Leont'eva-Smirnova, Dislocation density evolution in the process of high-temperature treatment and creep of EK-181 steel, Mater. Charact. 125 (2017) 23–28.
[66] F. HajyAkbary, J. Sietsma, A.J. Böttger, M.J. Santofimia, An improved X-ray diffraction analysis method to characterize dislocation density in lath martensitic structures, Mater. Sci. Eng. A 639 (2015) 208–218.
[67] S. Takebayashi, T. Kunieda, N. Yoshinaga, K. Ushioda, S. Ogata, Comparison of the dislocation density in martensitic steels evaluated by some X-ray diffraction methods, ISIJ Int. 50 (6) (2010) 875–882.

[68] F. Christien, M. Telling, K. Knight, Neutron diffraction in situ monitoring of the dislocation density during martensitic transformation in a stainless steel, Scr. Mater. 68 (7) (2013) 506–509.
[69] G. Speich, H. Warlimont, Yield strength and transformation substructure of low-carbon martensite, J. Iron Steel Inst. 206 (4) (1968) 385–392.
[70] B. Hutchinson, J. Hagström, O. Karlsson, D. Lindell, M. Tornberg, F. Lindberg, M. Thuvander, Microstructures and hardness of as-quenched martensites (0.1–0.5% C), Acta Mater. 59 (14) (2011) 5845–5858.
[71] B. Kim, E. Boucard, T. Sourmail, D. San Martín, N. Gey, P. Rivera-Díaz-del Castillo, The influence of silicon in tempered martensite: understanding the microstructure–properties relationship in 0.5–0.6 wt.% c steels, Acta Mater. 68 (2014) 169–178.
[72] H. Ghassemi-Armaki, R. Chen, K. Maruyama, M. Yoshizawa, M. Igarashi, Static recovery of tempered lath martensite microstructures during long-term aging in 9–12% Cr heat resistant steels, Mater. Lett. 63 (28) (2009) 2423–2425.
[73] T. Swarr, G. Krauss, The effect of structure on the deformation of as-quenched and tempered martensite in an Fe-0.2 pct C alloy, Metall. Trans. A 7 (1) (1976) 41–48.
[74] G.I. Taylor, The mechanism of plastic deformation of crystals. part i.theoretical, Proc. R. Soc. London Ser. A Containing Pap. Math. Phys. Charact. 145 (855) (1934) 362–387.
[75] J. Rosenberg, H. Piehler, Calculation of the taylor factor and lattice rotations for bcc metals deforming by pencil glide, Metall. Trans. 2 (1) (1971) 257–259.
[76] D. Simonovic, C.K. Ande, A.I. Duff, F. Syahputra, M.H.F. Sluiter, Diffusion of carbon in bcc Fe in the presence of Si, Phys. Rev. B 81 (5) (2010) 054116, https://doi.org/10.1103/PhysRevB.81.054116.
[77] F. Maresca, V. Kouznetsova, M. Geers, Subgrain lath martensite mechanics: anumerical–experimental analysis, J. Mech. Phys. Solids 73 (2014) 69–83.
[78] P. Andric, W. Curtin, Atomistic modeling of fracture, Modell. Simul. Mater. Sci. Eng. 27 (1) (2018) 013001.
[79] T.C.-t. Ting, T.C.-t. Ting, Anisotropic Elasticity: Theory and Applications Vol. 45, Oxford University Press on Demand, 1996.
[80] Z. Wu, B. Yin, W. Curtin, Energetics of dislocation transformations in hcp metals, Acta Mater. 119 (2016) 203–217.
[81] A. Stroh, Dislocations and cracks in anisotropic elasticity, Philos. Mag. 3 (30) (1958) 625–646.
[82] T. TC, Anisotropic Elasticity: Theory and Applications, Oxford University Press, 1996.
[83] J.D. Eshelby, The elastic field outside an ellipsoidal inclusion, Proc. R. Soc. Lond. A 252 (1271) (1959) 561–569.
[84] P. Andric, B. Yin, W. Curtin, Stress-dependence of generalized stacking fault energies, J. Mech. Phys. Solids 122 (2019) 262–279.
[85] M. Vasoya, B. Kondori, A.A. Benzerga, A. Needleman, Energy dissipation rate and kinetic relations for Eshelby transformations, J. Mech. Phys. Solids 136 (2020) 103699.
[86] E. Clouet, C. Varvenne, T. Jourdan, Elastic modeling of point-defects and their interaction, Comput. Mater. Sci 147 (2018) 49–63.
[87] K. Ingebrigtsen, A. Tonning, Elastic surface waves in crystals, Phys. Rev. 184 (4) (1969) 942.
[88] A.P. Sutton, R.W. Balluffi, Interfaces in Crystalline Materials, Clarendon Press, Oxford, 1995.citeulike-article-id:811528
[89] S. Morito, J. Nishikawa, T. Maki, Dislocation density within lath martensite in Fe-C and Fe-Ni alloys, ISIJ Int. 43 (9) (2003) 1475–1477, https://doi.org/10.2355/isijinternational.43.1475.
[90] J. Cheng, J. Luo, K. Yang, Aimsgb: an algorithm and open-source python library to generate periodic grain boundary structures, Comput. Mater. Sci 155 (July) (2018) 92–103, https://doi.org/10.1016/j.commatsci.2018.08.029.
[91] A. Hjorth Larsen, J. Jørgen Mortensen, J. Blomqvist, I.E. Castelli, R. Christensen, M. Dułak, J. Friis, M.N. Groves, B. Hammer, C. Hargus, E.D. Hermes, P. C. Jennings, P. Bjerre Jensen, J. Kermode, J.R. Kitchin, E. Leonhard Kolsbjerg, J. Kubal, K. Kaasbjerg, S. Lysgaard, J. Bergmann Maronsson, T. Maxson, T. Olsen, L. Pastewka, A. Peterson, C. Rostgaard, J. Schiøtz, O. Schütt, M. Strange, K. S. Thygesen, T. Vegge, L. Vilhelmsen, M. Walter, Z. Zeng, K.W. Jacobsen, The atomic simulation environmenta Python library for working with atoms, J. Phys. Condens. Matter 29 (27) (2017) 273002, https://doi.org/10.1088/1361-648X/aa680e.
[92] S. Plimpton, Fast parallel algorithms for short-range molecular dynamics, J. Comput. Phys. 117 (1) (1995) 1–19, https://doi.org/10.1006/jcph.1995.1039.
[93] G.J. Ackland, M.I. Mendelev, D.J. Srolovitz, S. Han, A.V. Barashev, Development of an interatomic potential for phosphorus impurities in -iron, J. Phys. Condens. Matter 16 (27) (2004) S2629–S2642, https://doi.org/10.1088/0953-8984/16/27/003.
[94] A. Stukowski, Visualization and analysis of atomistic simulation data with OVITO–the open visualization tool, Modell. Simul. Mater. Sci. Eng. 18 (1) (2009) 015012.
[95] A. Stukowski, V.V. Bulatov, A. Arsenlis, Automated identification and indexing of dislocations in crystal interfaces, Modell. Simul. Mater. Sci. Eng. 20 (8) (2012) 085007.
[96] A. Stukowski, K. Albe, Extracting dislocations and non-dislocation crystal defects from atomistic simulation data, Modell. Simul. Mater. Sci. Eng. 18 (8) (2010) 085001.
[97] P. Hohenberg, W. Kohn, Inhomogeneous electron gas, Phys. Rev. 136 (3B) (1964) B864–B871, https://doi.org/10.1103/PhysRev.136.B864.
[98] W. Kohn, L.J. Sham, Self-consistent equations including exchange and correlation effects, Phys. Rev. 140 (4A) (1965) A1133–A1138, https://doi.org/10.1103/PhysRev.140.A1133.
[99] M. Torrent, F. Jollet, F. Bottin, G. Zérah, X. Gonze, Implementation of the projector augmented-wave method in the ABINIT code: application to the study of iron under pressure, Comput. Mater. Sci 42 (2) (2008) 337–351, https://doi.org/10.1016/j.commatsci.2007.07.020.
[100] P.E. Blöchl, Projector augmented-wave method, Phys. Rev. B 50 (24) (1994) 17953–17979, https://doi.org/10.1103/PhysRevB.50.17953.
[101] K.F. Garrity, J.W. Bennett, K.M. Rabe, D. Vanderbilt, Pseudopotentials for high-throughput DFT calculations, Comput. Mater. Sci. 81 (2014) 446–452, https://doi.org/10.1016/j.commatsci.2013.08.053.
[102] X. Gonze, B. Amadon, P.M. Anglade, J.M. Beuken, F. Bottin, P. Boulanger, F. Bruneval, D. Caliste, R. Caracas, M. Côté, T. Deutsch, L. Genovese, P. Ghosez, M. Giantomassi, S. Goedecker, D.R. Hamann, P. Hermet, F. Jollet, G. Jomard, S. Leroux, M. Mancini, S. Mazevet, M.J.T. Oliveira, G. Onida, Y. Pouillon, T. Rangel, G.M. Rignanese, D. Sangalli, R. Shaltaf, M. Torrent, M.J. Verstraete, G. Zerah, J.W. Zwanziger, ABINIT: first-principles approach to material and nanosystem properties, Comput. Phys. Commun. 180 (12) (2009) 2582–2615, https://doi.org/10.1016/j.cpc.2009.07.007.
[103] J.P. Perdew, K. Burke, M. Ernzerhof, Generalized gradient approximation made simple, Phys. Rev. Lett. 77 (18) (1996) 3865–3868, https://doi.org/10.1103/PhysRevLett.77.3865.
[104] A.D. Becke, Density-functional exchange-energy approximation with correct asymptotic behavior, Phys. Rev. A 38 (6) (1988) 3098–3100, https://doi.org/10.1103/PhysRevA.38.3098.
[105] D.C. Langreth, M.J. Mehl, Beyond the local-density approximation in calculations of ground-state electronic properties, Phys. Rev. B 28 (4) (1983) 1809–1834, https://doi.org/10.1103/PhysRevB.28.1809.
[106] J.P. Perdew, J.A. Chevary, S.H. Vosko, K.A. Jackson, M.R. Pederson, D.J. Singh, C. Fiolhais, Atoms, molecules, solids, and surfaces: applications of the generalized gradient approximation for exchange and correlation, Phys. Rev. B 46 (11) (1992) 6671–6687, https://doi.org/10.1103/PhysRevB.46.6671.
[107] J.P. Perdew, J.A. Chevary, S.H. Vosko, K.A. Jackson, M.R. Pederson, D.J. Singh, C. Fiolhais, Erratum: atoms, molecules, solids, and surfaces: applications of the generalized gradient approximation for exchange and correlation, Phys. Rev. B 48 (7) (1993) 4978, https://doi.org/10.1103/PhysRevB.48.4978.2.
[108] E. Bitzek, P. Koskinen, F. Gähler, M. Moseler, P. Gumbsch, Structural relaxation made simple, Phys. Rev. Lett. 97 (17) (2006) 1–4, https://doi.org/10.1103/PhysRevLett.97.170201.
[109] S. Echeverri Restrepo, M.H. Sluiter, B.J. Thijsse, Atomistic relaxation of systems containing plasticity elements, Comput. Mater. Sci. 73 (2013) 154–160, https://doi.org/10.1016/j.commatsci.2013.03.001.
[110] P. Haas, F. Tran, P. Blaha, Calculation of the lattice constant of solids with semilocal functionals, Phys. Rev. B Condensed Matter Mater.Phys. 79 (8) (2009) 1–10, https://doi.org/10.1103/PhysRevB.79.085104.
[111] D.H.R. Fors, G. Wahnström, Theoretical study of interface structure and energetics in semicoherent Fe(001)/MX(001) systems (M=Sc, Ti, V, Cr, Zr, Nb, Hf, Ta; X=C or N), Phys. Rev. B 82 (19) (2010) 195410, https://doi.org/10.1103/PhysRevB.82.195410.
[112] A. Hung, I. Yarovsky, J. Muscat, S. Russo, I. Snook, R. Watts, First-principles study of metallic iron interfaces, Surf. Sci. 501 (3) (2002) 261–269, https://doi.org/10.1016/S0039-6028(01)01762-9.
[113] W.P. Davey, Precision measurements of the lattice constants of twelve common metals, Phys. Rev. 25 (6) (1925) 753–761, https://doi.org/10.1103/PhysRev.25.753.
[114] N. Ridley, H. Stuart, Lattice parameter anomalies at the Curie point of pure iron, J. Phys. D Appl. Phys. 1 (10) (2002) 1291–1295, https://doi.org/10.1088/0022-3727/1/10/308.
[115] S. Echeverri Restrepo, D. Di Stefano, M. Mrovec, A.T. Paxton, Density functional theory calculations of iron - vanadium carbide interfaces and the effect of hydrogen, Int. J. Hydrogen Energy 45 (3) (2020) 2382–2389, https://doi.org/10.1016/j.ijhydene.2019.11.102.